THESIS

SENSITIVITY OF SIMULATED MICROPHYSICS TO THE RAINDROP DISTRIBUTION SHAPE PARAMETER AND COMPARISONS WITH OBSERVATIONS

Submitted by

Kristen Van Valkenburg

Department of Atmospheric Science

In partial fulfillment of the requirements

For the Degree of Master of Science

Colorado State University

Fort Collins, Colorado

Spring 2022

Master's Committee:

Advisor: Susan van den Heever
Co-Advisor: Steven Rutledge

Brenda Dolan
Richard Eykholt

ABSTRACT

SENSITIVITY OF SIMULATED MICROPHYSICS TO THE RAINDROP DISTRIBUTION SHAPE PARAMETER AND COMPARISONS WITH OBSERVATIONS

Representation of precipitation microphysics remains a challenge in numerical modeling. Model simulations using two-moment bulk microphysics require *a priori* choices, such as the rain size distribution shape parameter (ν), which is used to determine the width of the rain drop size distribution (DSD). Selection of ν is often somewhat arbitrary being due, in part, to a lack of observations on which to base such decisions. In this study, the sensitivity of rainfall characteristics to ν is assessed using numerical model simulations and compared with an observational data set. A continental deep convection (CD) case and a shallow maritime (MS) case are simulated using bin and bulk microphysical parameterizations. The model results show that accumulated precipitation in the MS case decreases 385% with increasing ν, while the CD case shows minimal variability. In the CD case, where both warm-, mixed-, and ice-phase microphysical processes are occurring, graupel mixing ratios and number concentrations show a monotonic decrease with increasing ν, while hail mixing ratios and number concentrations show a monotonic increase with increasing ν. An analysis of the microphysical processes comprising the rain budget reveals the MS case shows a shifting balance between evaporation and cloud water collection with changes in ν, with increasing evaporation being the predominant influence on decreased surface precipitation. In the CD case there is notable variability in a variety of microphysical processes including important feedbacks to ice species. Cloud water collection and evaporation are the greatest contributor in the CD simulations with lower rain shape

parameters. The value of ν greatly impacts contributions to the rain via melting of ice hydrometeors. As the value of ν increases, melting of ice species by collisions with rain decreases, and is near zero in the ν=10 simulation. Also, as ν increases, the rates of hail melting into rain increases. This analysis allows us to gain perspective into how the assumed rain ν in bulk microphysics parameterizations impacts both warm rain processes and feeds back onto mixed-phase and ice-phase processes.

In addition to the bulk parameterization sensitivity tests, both cases are also simulated using a bin microphysics scheme, where the hydrometeor size distributions are allowed to freely evolve throughout the simulation. Using appropriate fitting approaches, we evaluate the range of rain shape parameters predicted in both cases as well as the variability of ν values throughout the three-dimensional storm structure.

The microphysical processes and rainfall characteristics of the bulk simulations are also evaluated relative to disdrometer observations using a previously developed 2D phase space of the intercept parameter ($\log N_w$) and median drop diameter (D_0). In this framework, lower ν values in the bulk microphysics MS case correspond more closely with observations, while in the CD case, higher ν correspond more closely with observations. These findings demonstrate the sensitivity of those assumptions constraining rain DSDs in microphysical parameterizations and provide a model-to-observation comparisons to help guide *a priori* choices of ν necessary for more accurate simulations utilizing bulk microphysics schemes.

ACKOWLEDGEMENTS

I'd like to give a great thank you to all of the friends and family who supported me through this journey of research and writing. The continued optimism and encouragement fueled me through this process. A special thank you to my husband, for steadfast endurance through my entire education. Mom and Dad, thank you for fostering curiosity and the courage to challenge myself.

Thank you to my entire committee for your time and dedication to me and this work. The collaboration of this research is important and profound, so thank you for allowing me to be a part of it. Specifically, Brenda Dolan, who is the engine who keeps us moving, I am grateful for the extra support and encouragement you are always quick to provide. To the van den Heever and Rutledge Research Groups, I am grateful to work next to such brilliant minds who challenge me and simultaneously make me laugh.

I'd like to acknowledge funding from the Department of Energy, Atmospheric Science Research grant DE-SC0017977. High performance computing support provided by the Department of Energy Stratus Supercomputer. Thank you to the creators of PyDSD, Joseph Hardin and Nick Guy (https://github.com/josephhardinee/PyDSD/tree/v1.0) and to Adele Igel for her insights and HUCM-BIN simulation support.

TABLE OF CONTENTS

CHAPTER 1 INTRODUCTION

1.1 Introduction and Background

A thorough understanding of the hydrological cycle and patterns of freshwater on Earth is essential to understanding the past, present, and future climate and the challenges we may face due to changes in this cycle. Of the freshwater on Earth, only 0.04% of it is present in the atmosphere as water vapor, and yet precipitation is a fundamental process in the hydrological cycle (Shiklomanov, 1993). As the climate warms, it is expected that global drought conditions will increase due to decreases in regional precipitation combined with increased evaporation (Sheffield and Wood, 2008; Dai 2010). The other precipitation extreme, the production of localized heavy rainfall and associated flooding, is also expected to increase in a warmer climate due to more water vapor being present in the atmosphere (Schumacher, 2017). Both precipitation extrema pose challenges for life on Earth. An enhanced understanding of cloud processes and improved forecasting of precipitation is therefore essential to adapt to the climate-induced precipitation challenges we will face on timescales of minutes to decades. To achieve this understanding, improving the capability to accurately represent precipitation processes in numerical models is essential.

In order to understand the characteristics of the precipitation occurring at the surface, we must understand the many microphysical processes occurring aloft that are responsible for its generation. These microphysical processes, such as condensation, evaporation, collision coalescence, melting, and riming, all occur on extremely small spatiotemporal scales, though the cloud systems facilitating these processes occur and impact local, regional and climate scales. One tool used to further our knowledge of processes generating precipitation are numerical

models. However, this juxtaposition of accurately representing processes occurring on a wide range of scales is one of the many challenges faced by numerical models.

As computational constraints make it impossible to model each individual hydrometeor within a convective storm system, microphysical processes and their associated collective impacts are represented using parameterizations. There are a number of different approaches utilized when parameterizing microphysical processes (Khain et al. 2015). One approach is the bulk microphysical approach. These schemes are typically single- or double-moment schemes, where one or two moments of the hydrometeor size distribution are predicted, respectively. In single moment schemes, often the mass is predicted (Koenig and Murray 1976; Lin et al. 1983; Rutledge and Hobbs 1984; Walko et al. 1995; Grabowski 1998; Xue et al. 2000; Morrison et al. 2009), while in double moment schemes, the mass and number concentration are typically predicted (Ferrier 1994; Meyers et al. 1997; Seifert and Beheng 2006; Morrison et al. 2009). Though less widely used, three-moment schemes are also available which typically predict radar reflectivity in addition to the mass and number concentration (Milbrandt and Yau 2005b; Paukert et al. 2019; Milbrandt et al. 2021). The size distribution of any hydrometeor type within a bulk microphysics parameterization is often determined using a generalized gamma distribution (Walko et al. 1995; Thompson et al. 2008; Morrison et al. 2009; Igel and van den Heever 2017a). The gamma size distribution is given as follows:

$$N(D) = \frac{N_T}{D_n^{\nu}\Gamma(\nu)} D^{\nu-1} e^{\frac{-D}{D_n}} \qquad \text{Eqn. 1}$$

where ν is the shape parameter (dimensionless); N_T is the total number concentration of hydrometeors in the grid volume ($\# \, m^{-3}$); D is the hydrometeor diameter (mm), which can

range from zero to infinity; D_n is the characteristic diameter of modified gamma distribution (mm); and Γ is the standard Euler gamma function (dimensionless). Therefore, $N(D)$ (m^{-4}) represents the number of hydrometeors per cubic meter per unit increment of diameter D.

Expressions representing hydrometeor size distributions, such as Eqn. 1, require *a priori* parameter settings to be made before the simulations are run. Selection of the values of such *a priori* parameters has been shown to impact precipitation within a simulation. For example, Morales at al. (2018) found that surface precipitation is affected by the *a priori* choice of the snow fall speed coefficient and snow particle density in an orographic environment. The sensitivity of precipitation to the choice in the diameter-fall speed relationship for ice hydrometeors in a supercell case was evaluated by Falk et al. (2019). They found higher ice hydrometeor fall speeds led to higher mixing ratios at lower levels, increased melting, and therefore, stronger downdrafts and surface cold pools. van den Heever and Cotton (2004) demonstrated that *a priori* choices in the mean hail diameter impact supercell precipitation and structures, thereby producing a change in supercell type from a classic supercell (Browning 1964; Lemon and Doswell 1979) to a high precipitation supercell (Doswell et al. 1990; Moller et al. 1994). The *a priori* selection of particle densities for the graupel/hail category has also been shown to have a significant impact on surface accumulated precipitation (Gilmore et al. 2004; Adams-Selin et al. 2013), and in a convective squall line case, the domain-mean precipitation rates tend to be higher with more efficient rain drop breakup parameterizations (Morrison et al. 2012). These studies demonstrate the importance of an appropriate selection of the *a priori* variables in order to more accurately represent the natural world and improve weather forecasting.

One such *a priori* parameter of importance in bulk microphysics schemes is the gamma distribution shape parameter, ν (Eqn. 1). In this study, we define ν as referring only to the raindrop size distribution shape parameter, though elsewhere it can be used to describe any hydrometeor size distribution shape parameter. Figure 1.1 illustrates sample rain drop size distributions (DSDs) calculated using the gamma expression (Eqn. 1), with various ν values and assuming a constant D of 1.0 mm and N_T of 20 cm^{-3}. Larger (smaller) values of ν correspond to narrower (broader) size distributions. The shape parameter ν therefore specifies the width of the size distribution, and in particular, the relative amounts of small to large hydrometeors. Several studies have examined the sensitivity of cloud processes and precipitation characteristics to changes in various hydrometeor shape parameter. Meyers et al. (1997) found that accumulated precipitation tripled within simulated convection when ν was increased from 1 to 3. Milbrandt and Yau (2005a) noted that in a two-moment bulk microphysics scheme, the selection of ν played an important role in the rate of size sorting of rain. Igel and van den Heever (2017a) found that variations in the cloud shape parameter had an impact on condensation and evaporation rates, with evaporation being most affected. Finally, Freeman et al. (2019) observed that accumulated precipitation in a simulated deep convective storm was impacted up to 75% based on the selection of ν. While Freeman et al. (2019) investigated the sensitivities to ν within a single case of deep convection, they did not analyze the impacts of the rain shape parameter on ice phase processes, nor did they contrast these results with warm rain system processes.

As a result of the sensitivity of cloud and precipitation processes to the selection of ν, researchers and forecasters have turned to observations to help guide their ν selection. One of the first observations of rain DSDs was from Marshall and Palmer (1948). They concluded that higher rainfall rates were correlated with broader rain DSDs. Marshall and Palmer (1948) also

developed one of the frequently used forms of the gamma rain DSDs, the exponential distribution ($\nu 1$ in Fig. 1). However, since the studies of Marshall and Palmer (1948), other research has found that rain DSDs may not be exponential in shape, and that it may change throughout the storm lifetime (Uijlenhoet et al. 2003), as a function of storm type (Hooper et al. 2020), and with location within the storm (Bringi et al. 2003; Friedrich at al. 2015, 2016; Igel and van den Heever 2017b). The challenge of observing the full rain drop spectrum and fitting the data to a gamma distribution have further exacerbated the problem in assigning appropriate values for ν. As a result, a wide variety of often somewhat arbitrarily selected ν values have been used when modeling storm processes. Selecting appropriate values of ν for forecasting models is arguably even more challenging in that such settings are required to represent a wide range of cloud morphologies on any given day. Between the somewhat limited observations of rain DSDs and the previous sensitivity studies performed with numerical models, it is evident that additional work is needed to understand the impacts and feedbacks of the ν selection.

One of the alternatives to the *a priori* selection of ν is available through the use of bin microphysics schemes (Khain et al. 2015). Bin microphysics schemes explicitly represent hydrometeor size distributions using discrete size bins to predict hydrometeor properties within each bin, like mass and number. As such, bin microphysics schemes allow the shape of the rain DSDs to freely evolve over time and space, and therefore do not require *a priori* selection of a single ν. However, bin microphysics schemes are far more computationally expensive than bulk microphysics schemes, and are, therefore, less widely used than bulk microphysics schemes (Khain et al. 2015), but are growing in popularity with increasing computational capabilities.

The study presented here focuses on the impacts of the values of ν on precipitation, and warm and ice microphysics within both shallow and deep convection. To address this goal, both

bin and bulk microphysics schemes are used to simulate two disparate storm morphologies: a shallow, tropical maritime event and a continental deep convection event. This allows us to evaluate microphysical processes in warm and mixed phase cloud systems within the constraints of *a priori* ν, as well as situations where ν freely evolves. Lastly, we compare the precipitation characteristics of the numerically modeled precipitation to a global data set of disdrometer observations of surface precipitation analyzed by Dolan et al. (2018, herein D18). This research extends previous research into ν sensitivities, in particular that by Freeman et al. (2019), by examining ice-feedbacks in more detail, analyzing a shallow warm-rain only case, utilizing both bulk and bin parameterizations, and contextualizing the results against disdrometer observations.

FIGURES

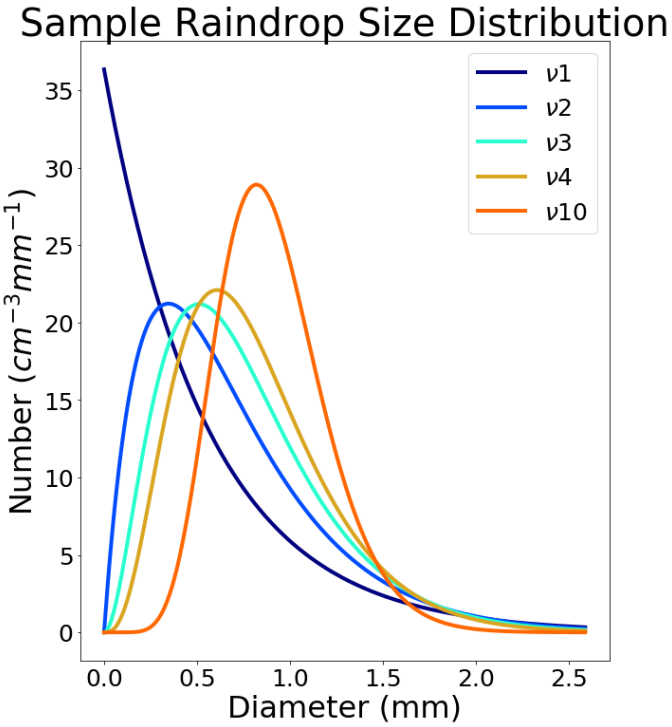

Figure 1.1: Sample rain drop size distributions as a result of changing ν. These distributions are determined using a constant mean mass diameter of 1.0 mm and a number concentration of 20 cm^{-3}.

CHAPTER 2 STUDY APPROACH

2. Study Approach

Both bulk and bin microphysics schemes were used to simulate two different storm morphologies in order to achieve the goals outlined in this study. The cases utilizing bulk microphysics are first evaluated to present the effects of ν on surface precipitation and warm- and cold-phase microphysical processes. The bin microphysics scheme is then used to help evaluate the spatial and temporal variability of ν as it is allowed to evolve, allowing comparison to the bulk model where ν is set to a single value. Finally, we compare the model simulations to surface observations of DSDs.

2.1 Case Studies

For the purpose of this study, sensitivity simulations were conducted in which ν was varied for two different storm morphologies. The shallow maritime event was chosen in order to investigate strictly warm rain microphysics (condensation and collision-coalescence), thereby allowing us to isolate the effects of ν on warm rain processes. The continental deep convection case facilitates an investigation into the impacts of ν on the microphysical processes occurring in ice and mixed phase clouds, in addition to those occurring within the warm phase.

An idealized simulation of a shallow maritime (MS) event was conducted, where the initial conditions were homogeneous in the horizontal direction and were comprised of a composite sounding gathered in the Atlantic Trade Wind Experiment (ATEX) (Augstein et al. 1973, 1974; Brümmer et al. 1974) (Fig. 2.1a). In order to initiate cloud formation, inhomogeneity was introduced using initial random surface potential temperature perturbations. ATEX has previously been used to examine trade wind boundary layer clouds (Albrecht 1979; Stevens et al.

2001,; Xue et al. 2008) and has been successfully simulated using RAMS (Saleeby et al. 2015). A 20 km x 20 km x 4 km model domain with grid spacing of 100-m in the horizontal and 50-m in the vertical was utilized. More information regarding the model configuration can be found in Table 2.1. This case study includes a cloud structure comprised of a layer of cumulus under stratocumulus (Saleeby et al. 2015). A vertical cross section of the total condensate for the MS case is presented in Figure 2.2a. Cloud top heights reach ~1.5 km, and remain entirely below the melting layer throughout the simulation duration, thereby providing an ideal case to examine warm rain microphysics exclusively.

The Continental Deep convection case (CD) is a high precipitation deep convection system initialized using a 2K thermal perturbation and with initial conditions following that of Weisman and Klemp (1982) (Fig. 2.1b). This event was selected in order to evaluate the sensitivity of both warm- and cold-phase processes to changes in ν, and the subsequent feedbacks between the two phases. RAMS has frequently been successfully used to simulate deep convection (e.g. Barth et al. 2007; Storer et al. 2010; Grant and van den Heever, 2014; Hosannah et al. 2015). The case selected for this study was analyzed in detail by Grant and van den Heever (2014). The simulation was run on a 285 km x 225 km x 24 km grid with 300-m grid spacing in the horizontal and a vertically stretched grid with spacing of 25-m near the surface and stretched to 300-m aloft at a ratio of 1.1. More information regarding the model configuration for this simulation can be found in Table 2.2. A vertical cross section of total condensate is presented in Figure 2.2b. Cloud top heights reach ~14 km, with portions of the system occurring at, above, and below the melting layer allowing for the analysis of warm-, mixed-, and ice- phase microphysical processes.

2.2 Model Setup and Experiments

Twelve high resolution numerical model simulations were performed, ten of which utilize a bulk microphysics scheme, and two of which utilize a bin microphysics scheme. The Regional Atmospheric Modeling System (RAMS) (Cotton et al. 2003; Saleeby and van den Heever, 2013) was used to conduct all of the simulations. RAMS is a non-hydrostatic mesoscale model which includes sophisticated aerosol, microphysical and land surface parameterizations. It has been used to simulate a variety of storm morphologies (Castro et al. 2005, 2007; Grant and van den Heever 2014; Federico et al. 2014; Hosannah et al. 2015; Marinescu et al. 2017; Park et al. 2020; Riley Dellaripa et al. 2020). The RAMS two-moment bulk microphysics scheme predicts the mixing ratio and number concentration of eight hydrometeor types: cloud, drizzle, rain, pristine ice, snow, aggregates, graupel, and hail (Meyers et al. 1997).

Both the MS and CD storm morphologies are simulated using a range of ν values typical of those frequently used within the community and measured in observations (Meyers et al. 1997; Uijlenhoet et al. 2003; Milbrandt and Yau 2005a; Siefert 2008; Nui et al. 2010; Thurai and Bringi 2018). Values of ν =1, 2, 3, 4, and 10 are utilized in our numerical experiments (Fig. 1.1). For each storm morphology case, the simulations are identical other than the *a priori* specification of ν. Herein, each case will be denoted as either the maritime shallow (MS) or continental deep (CD), along with their respective ν value. For example, the maritime shallow case with a ν of 1 will be designated as MSν1. Details of this nomenclature can be found in Table 2.2.

As stated above, an alternative to the requirement of setting ν *a priori* is the use of bin microphysics schemes, where the value of ν is allowed to freely evolve in space and time. The Hebrew University Cloud Model Spectral Bin Microphysics Model (HUCM-BIN) version 6.1.20

(Khain et al. 2004), which has been implemented into RAMS (Igel and van den Heever 2017b), was used for these experiments. This allows for the same RAMS dynamical core to be used in simulations with either bulk or bin microphysics. Ice species fall speeds within the HUCM-BIN simulations have been updated based on the findings of Falk et al. (2019). All of the other model settings, with the exception of the microphysical parameterizations, are identical to the bulk microphysics simulations for both storm morphologies. The case studies using HUCM-BIN will be referred to as MS-BIN or CD-BIN.

To estimate the value of ν from the size distributions that result from the bin microphysics simulations, we employed a distribution fitting algorithm to the bin simulations. We used the open-source Python package, PyDSD (version 1.0.6.2), which was specifically developed for handling disdrometer and particle probe drop size distribution data and uses a minimization of the mean square error of an assumed gamma distribution (Hardin and Guy, 2017). We modified PyDSD to fit a gamma distribution to the rain distribution at each grid point throughout the entire simulation for both BIN-MS and BIN-CD. In this way, we could uncover what the bin simulations would predict ν to be at each point in space and time, and subsequently compare the results to the *a priori* ν applied in the bulk microphysics simulations. It should be noted that PyDSD allows for a range of possible ν values with a lower limit of -5 (super-exponential) and an upper limit of 21. The use of the bin schemes also allows us to follow the evolution of ν in time and space, thereby obtaining a better understanding of the DSD variability which would occur in the natural world.

While bin microphysics parameterizations are typically viewed as the more sophisticated, advanced approach compared with bulk schemes (Khain et al. 2015), they are computationally expensive and therefore not always feasible for long duration simulations. For example, in this

study the CD case was simulated on the Department of Energy (DOE) Stratus Supercomputer. The simulation length is three hours. Using 360 processors, the bulk microphysics simulation took 4 wall-clock hours to complete. The same CD simulation, on the same supercomputer and using the same number of processors, but with the bin microphysics scheme, took 75 wall-clock hours to complete. Khain et al. (2015) states bin microphysics approaches may require five to twenty times more computer time than current bulk parametrization schemes, a fact supported by the simulations conducted here. When available, a bin microphysics scheme has obvious advantages, however the practicality and efficiency of bulk simulations means they are still widely employed. Therefore, a guide to the appropriate selection of ν and the associated microphysical feedbacks, such as we seek in this study, is insightful.

2.3 Model-Observation Comparisons

We also undertook a comparison of the model simulations with field observations to evaluate the performance of the models. Application of a previously developed multi-parameter comparison framework allows us to compare the simulated surface rain characteristics to those measured and recorded in an extensive, global disdrometer data set (D18). Using Principal Component Analysis (PCA), D18 analyzed six different variables from the global disdrometer data set. Distinct modes of co-variability emerged and are hypothesized to be related to different microphysical processes that occurred aloft to produce the rain DSDs measured at the surface. Dolan et al. (2021) have further expanded the use of this unique framework to include an analysis of the same six precipitation variables resulting from a diverse set of RAMS simulations, two of which are the cases used in this study. Here, we take a similar approach and analyze the case studies herein in the 2-D phase space of the log of the intercept parameter ($\log N_w$) and median drop diameter (D_0). This facilitates an examination of the sensitivity of ν in

this framework elucidating a multi-parameter comparison of the model results to observational measurements.

2.4 Microphysical Process Rates

RAMS has the capability to output 3D microphysical process rates for most of the parameterized microphysical processes, including autoconversion, accretion, condensation, evaporation, deposition, sublimation, collisional melting, thermodynamic melting, riming of cloud water, rain accretion by ice species, and ice crystal aggregation. Here we will focus on the processes involved with generating or removing rain in both cases. Process rates are initially cumulative mixing ratios in units of g $kg^{-1}s^{-1}$, and we present these values in units of kg to account for the summation over space and time and the density of water. This allows for evaluating the amount of water, or water equivalent for ice hydrometeors, transferred to and from each hydrometeor category over the entire domain and simulation.

RAMS also computes the hydrometeor internal energy, which allows for the individual calculation of melting and collision and coalescence terms (Walko et al. 1995). Many bulk microphysics schemes do not have such capabilities. Internal energy provides insight into the temperature of a hydrometeor, which is determined by latent heat release and absorption within each hydrometeor as well as sensible heat from collisions between hydrometeors. RAMS utilizes a heat budget for each hydrometeor category that is based on the mean category temperature, the specific heat of ice and water, and the latent heat of fusion of water. This study will utilize the internal energy of rain to explore the sensitivity of collisional melting of ice hydrometeors and thermodynamic melting of hail to ν.

In the MS case, the processes that contribute to the rain budget are cloud water collection and condensation/evaporation. Cloud water collection includes autoconversion (cloud drops

colliding and coalescing into larger drops) and cloud water accreted by rain. Condensation and evaporation are represented as a single combined term where positive values correspond to net condensation and negative values correspond to net evaporation. For the CD case, there are numerous microphysical process rates involved in the rain budget. The sources of rain are cloud water collection, condensation, collisional melting of all ice species, and the melting of aggregates, graupel, hail, and snow, each of which are represented by their own term. Cloud water collection is the same as described for the MS case above. Collisional melting refers to rain generated by the collision of an ice hydrometeor with rain that initiates melting. The aggregates, graupel, hail, and snow melting terms refer to the thermodynamic melting of these hydrometeors. The sinks of the rain budget remove liquid from the rain category and are as follows: evaporation (as described above), and the riming (and subsequent freezing) of rain water by pristine ice, snow, aggregates, graupel, and hail, each of which is represented by their own term.

TABLES AND FIGURES

Table 2.1: RAMS model configurations for both MS and CD cases.

Maritime Shallow (MS)	Grid	Δx = 100 m (20km x 20km); Δz = 50 m
	Initial Conditions	Composite ATEX sounding (Augstein et al 1973, 1974; Brümmer et al. 1974). Horizontally homogeneous
	Initialization	Random surface potential temperature perturbation.
	Microphysics	RAMS bin-emulating two-moment bulk microphysics version 6.2.12 (Walko et al. 1995; Saleeby and Cotton 2004; Saleeby and van den Heever 2013). HUCM-BIN (Khain et al. 2004) implemented into RAMS (Igel and van den Heever 2017b)
	Time	9 hours; Δt= 1 second
	Boundary Conditions	Lateral: cyclic; Top: upper 5 layers Rayleigh friction absorbing; Bottom: Ocean surface (298K).
Continental Deep (CD)	Grid	Δx = 300 m (285km x 225km); Δz=25 m at the surface; stretched to 300 m over 91 vertical levels (~24km) with a stretching ratio of 1.1
	Initial Conditions	Weisman and Klemp (1982) sounding
	Initialization	2K thermal perturbation
	Microphysics	RAMS bin-emulating two-moment bulk microphysics version 6.1.18 (Walko et al. 1995; Saleeby and Cotton 2004; Saleeby and van den Heever 2013). HUCM-BIN (Khain et al. 2004) implemented into RAMS (Igel and van den Heever 2017b) with updated ice species fall speeds (Falk et al 2019)
	Time	3 hours; Δt= 1 second
	Boundary Conditions	Lateral: open radiatively (Klemp and Wilhelmson 1978); Top: upper 6 layers Rayleigh friction absorbing; Bottom: Free slip with short grass surface vegetation
Both	Turbulence	Smagorinksy (1963) turbulence in the vertical and horizontal
	Aerosol Radiation	None

Table 2.2: Nomenclature for each case and its respective rain shape parameter value and microphysics scheme.

Storm Type	Bulk Microphysics Rain Shape Parameter Value					Bin Microphysics
	ν=1	ν=2	ν=3	ν=4	ν=10	
Maritime Shallow Convection	MSν1	MSν2	MSν3	MSν4	MSν10	MS-BIN
Continental Deep Convection	CDν1	CDν2	CDν3	CDν4	CDν10	CD-BIN

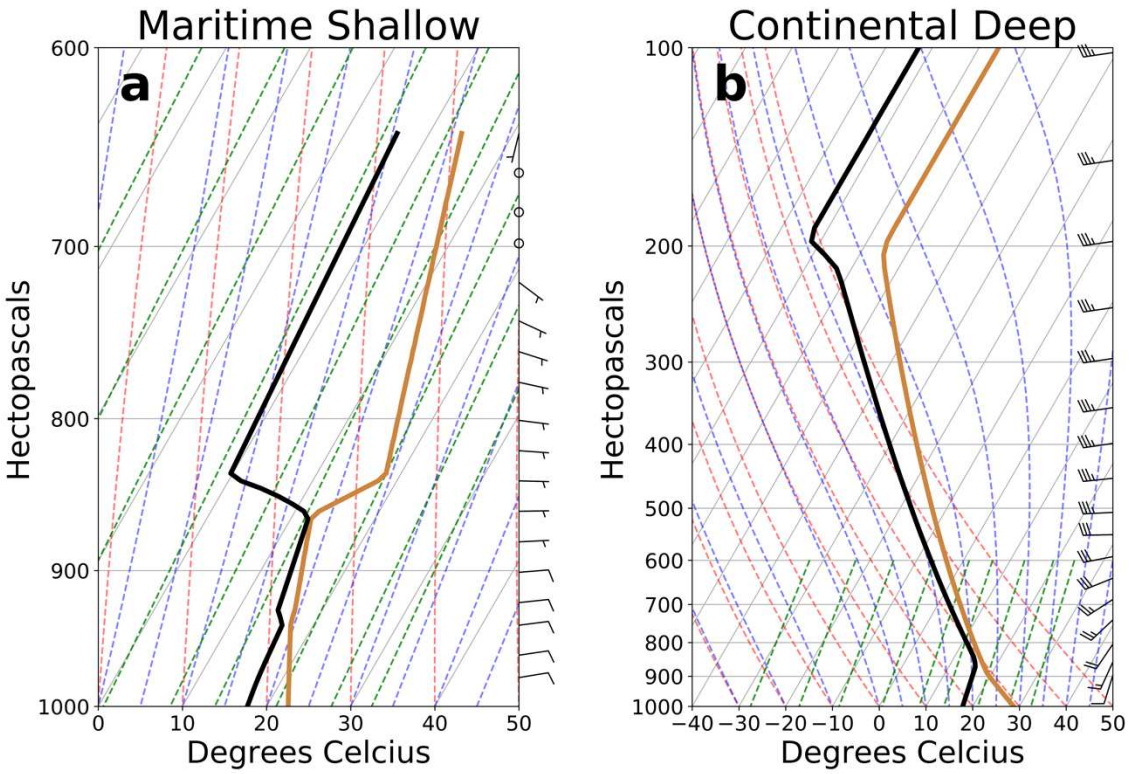

Figure 2.1: (a) MS and (b) CD soundings used to initialize the modeling sensitivity studies.

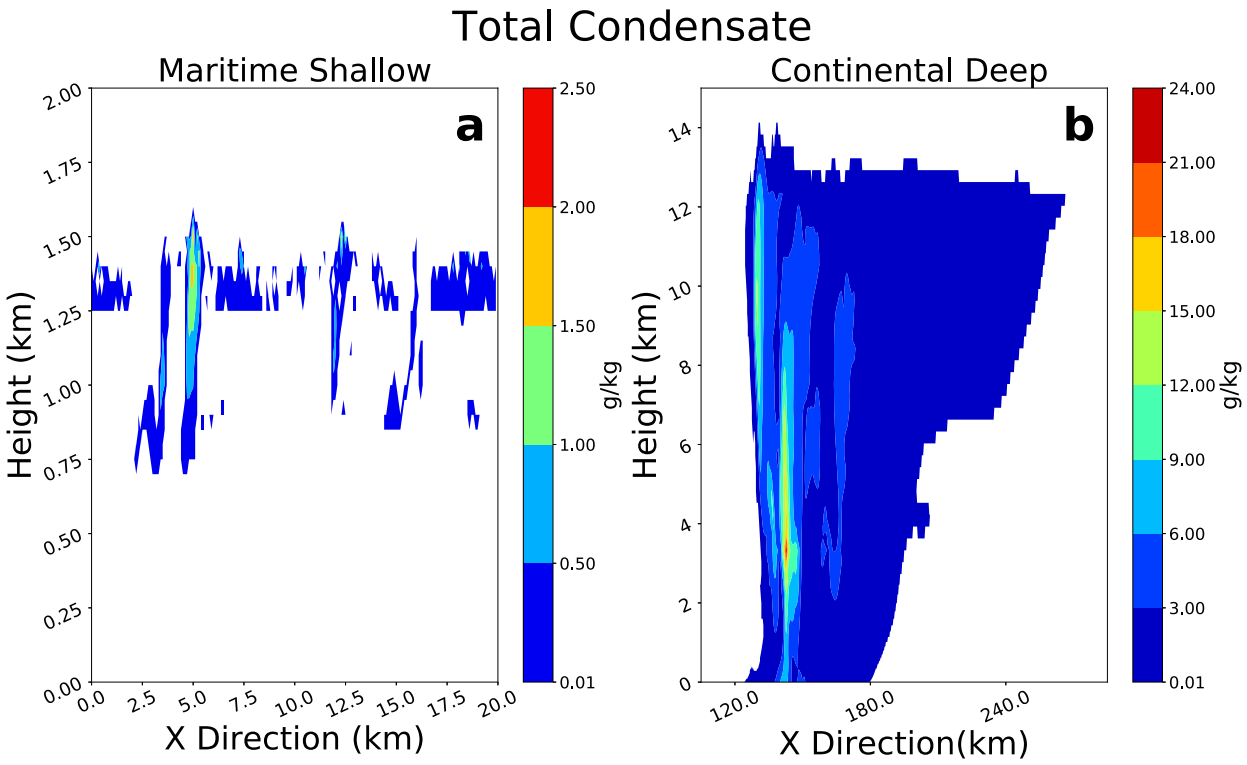

Figure 2.2: Vertical cross-section of total condensate (g/kg) of (a) MS case and (b) CD case through the point of maximum total condensate.

CHAPTER 3 RESULTS

3.1 Precipitation and Hydrometeor Characteristics

3.1.1 Accumulated Precipitation

We begin by examining the trends in accumulated precipitation at the surface for both cases (Fig. 3.1). The total accumulated precipitation (kg) is calculated by summing the rain mixing ratio over the domain (kg m^{-2}) and multiplying by the total area of the domain (m^2). It is evident that the amount of accumulated precipitation in the MS case decreases significantly with increasing ν (Fig. 3.1a). The $\nu 1$ simulation produced 385% more accumulated surface precipitation than the $\nu 10$ simulation. The MS case also demonstrates sensitivity in the spatial distribution of surface accumulated precipitation with increased ν (Fig. 3.2a-e). Higher values of ν (a narrower rain DSD) correspond to lower overall accumulated surface precipitation, with the precipitation reaching the surface favoring the southern portion of the domain. Narrower rain DSDs have an increased number of similarly sized drops, which are less likely to collide to form larger drops because of similar fall velocities. Because of this decreased collision efficiency, raindrop sizes are smaller, allowing for more efficient evaporation. This weakened the areas of more intense precipitation in the southern portion of the domain, and eliminated the already weak areas of precipitation in the northern portion of the domain with increases in ν. The processes associated with this precipitation distribution are examined in more detail in Sec. 3.2.1.

The value of ν appears to have less of an impact on the accumulated precipitation produced in the CD case (Fig. 3.1b) when compared with the MS case. The magnitudes only differ by ~5% with variations in $\nu 1$ through $\nu 4$. However, the $\nu 10$ simulation produces ~11% more surface precipitation than the other simulations, primarily towards the end of the simulation. This is caused by hail accumulating at the surface, which is unique to this simulation,

and will be further investigated in Section 3.2. In contrast, Freeman et al. (2019) found that the amount of accumulated rainfall at the surface in the supercell case that they simulated changed by 200% over ν values of 1-10 (Freeman et al. 2019, Fig. 7). The differences between these two studies are a result of significantly more liquid water being available to the storm within our CD environmental initialization. More liquid water decreases the influence of evaporation acting on raindrops, which was one of the main processes attributed to the changes in accumulated rainfall in Freeman et al. (2019). This highlights the role of the environment in modulating the sensitivities to ν.

Spatially, the overall structure of accumulated precipitation did not differ significantly in the CD case as ν was varied (Fig. 3.2f-j). All simulations within the CD case depict splitting deep convection with both a distinct left and right mover as the system propagates from left to right across the domain. The structure of accumulated precipitation in the left-mover experiences the most change as ν increases. Most notably, in the ν10 simulation, the left mover has significant increases in the amount of precipitation produced, although it is distributed over a slightly smaller area. This is due to hail accumulating at the surface. There are only small changes to precipitation accumulating from the right-mover. Interestingly, a much larger sensitivity of the precipitation produced by the left-mover to changes in the mean hail diameter size were also observed in van den Heever and Cotton (2004), and points to the role of the cold pools. Cold pools are also impacted by changes to the microphysics, and their subsequent support of the updraft. However, as our focus is on the microphysical processes, we leave a detailed analysis of the storm dynamics for another study.

In summary, the sensitivity of accumulated precipitation at the surface to ν varies as a function of storm type and the environment. In the MS case, as ν increases, the amount of

accumulated precipitation decreases and the precipitation is concentrated toward the southern portion on the domain. In the CD case, the overall amount of accumulated precipitation does not vary significantly in this case, except for the $\nu 10$ simulation where hail reaches the surface. This is in contrast to Freeman et al. (2019) who found a much larger change in precipitation amounts as a function of ν in their drier supercell environment. The precipitation produced by the left-mover of the CD case does, however, show greater variability than that of the right-mover, most notably in the $\nu 10$ simulation. Overall, the sensitivity of accumulated precipitation to ν is dependent on the storm morphology and environment, with the weaker MS case being more significantly impacted than the more dynamically-driven moist CD case.

3.1.2 Rain Rate Characteristics

Another important element of surface precipitation, particularly for flash flooding events, is the rainfall rate. Here, we examine the sensitivity of rainfall rates to variations in ν for each of the cases (Fig. 3.3). The MSν1 simulation shows the highest frequency of rain rates near 0.1 mm hr^{-1}, with MSν10 following closely behind (Fig. 3.3a). Both of these distributions have an ample number of small drops (Fig. 3.4a, e, i). Evaporation can act more efficiently on small drops which will lead to a greater frequency of lower rain rates. MSν3 and MSν4 have the highest frequency from 1-10 mm hr^{-1}, representing more moderate to heavy rainfall rates for this type of storm morphology. For MSν3-4, which represent broader distributions, more moderately-sized drops will develop and precipitate relatively quickly.

In the CD case there are differences in the maximum frequency and in the frequency of the largest rain rates (Fig. 3.3b). All of the simulations have their respective maximum frequencies occurring in moderate rain rates (20-40 mm hr^{-1}), with CDν2-4 having the greatest frequencies. CDν10 has the highest frequency of rain rates greater than 40 mm hr^{-1}. This

enhanced rain rate is caused by the increased amount of hail that is available for melting into rain within this simulation, unlike the other simulations. We analyze the hail related processes in more detail in section 3.2.2.

Though simple, monotonic trends in surface rain rate do not occur in either case, it is important to try to unpack the complex feedbacks impacting surface rain rates occurring in both cases. When only warm rain processes are occurring in the MS case, the broader distributions (MSν3-4), have the highest frequency of moderate rain rates. In the CD case, where melting of ice contributes to the rain rate, the CDν10 simulation has the highest frequency of large rain rates. A detailed investigation into the processes responsible for these ν-impacts on the precipitation rates is included below.

3.1.3 Hydrometeor Characteristics

Examining the general hydrometeor characteristics such as mixing ratio and number concentration, which are predicted in this two-moment bulk microphysics scheme, provides information on the direct impacts that ν may have on the population of various types of hydrometeors. Figure 3.4 presents the mean hydrometeor number concentration, mixing ratio, and diameter as a function of height for rain in the MS case and for rain, graupel, and hail in the CD case. Values are horizontally averaged over the domain and the duration of the simulation. Only points in the domain with mixing ratios greater than 0.1 g kg^{-1} are included in the mean. We recognize that details can be hidden by taking a mean profile, but this method also provides an overall understanding of the hydrometeor characteristics.

In the MS case, there is a clear monotonic increase in rain drop number concentration and a corresponding decrease in the mass mean diameter as the value of ν increases (Fig. 3.4a, i). Due to the nature of the gamma distribution, as ν increases, there is an increased number of

drops around the mass mean diameter, and a reduced drop number concentration away from the mean mass diameter. However, the trend in the rain mixing ratio as ν increases is non-monotonic, and represents an interesting scenario comprised of two different regimes, one in which mixing ratio decreases towards the surface ($\nu 1$, $\nu 2$) and one in which the mixing ratio increases towards the surface ($\nu 4$, $\nu 10$), with $\nu 3$ representing a mix of the two (Fig. 3.4e). These trends emerge due to changes in evaporation rates, and are enhanced in this figure because we are showing the mean, which must meet the above stated rain mixing ratio thresholds to be included. Evaporation will be examined in the following section (sec. 3.2) when microphysical process rates are discussed.

For the CD case, the rain hydrometeor characteristics as a function of ν differ in a variety of ways. First, the number concentration generally decreases with decreasing ν, with the peaks occurring at slightly lower altitudes with smaller ν (Fig. 3.4b). As ν increases, there are more drops of a similar size to the mean mass diameter, and less drops larger than the mean mass diameter. Due to this, simulations with smaller ν are influenced by size sorting, where smaller drops remain higher aloft, while larger drops fallout more rapidly and therefore exist at lower altitudes. The mixing ratio trends for $\nu 1$ through $\nu 4$ are relatively consistent (Fig. 3.4f). However, the $\nu 10$ mixing ratio differs significantly from the other simulations, with much larger rain mixing ratios above ~4 km AGL, corresponding with the freezing level. At 4 km AGL, $\nu 10$ has the smallest rain mixing ratio and the largest mean sizes. Just above 2 km (near cloud base), the mixing ratio in the $\nu 10$ simulation begins to increase towards the surface while it decreases in the other simulations. As will be shown below, this pattern has to do with the role played by hail in this simulation. The mean rain diameters aloft are larger in the $\nu 10$ simulation due to the melting of ice hydrometeors. Towards the surface, all of the simulations have similar mean

diameters of ~1 mm, however, those in the ν10 are slightly larger (Fig. 3.4j). This is due to the broader distributions of the ν1-4 simulations, which allow for drops of different sizes that fall at different velocities, and are more likely to collide and initiate collisional breakup around 1 mm (Saleeby et al. 2021). The narrow distribution of the ν10 simulation has many drops of similar size, which fall at similar speeds, and are therefore less likely to collide to initiate breakup. This allows more drops of a larger size to reach the surface in the ν10 simulation. The analysis reveals that while the rain characteristics are relatively similar in the ν1-4 simulations, they are quite different in the ν10 simulation. The rain drop sizes are larger in almost all regions of the cloud, especially near the surface, and the rain mixing ratios are lofted higher in the cold-cloud regions compared to the other simulations. The processes responsible for these characteristics are described in the next section.

Examining the ice hydrometeor characteristics is necessary to understand the feedbacks between the rain and ice species as a result of the assumed ν. As the value of ν increases, both the graupel mixing ratio and number concentration decrease (Fig. 3.4 c,g respectively), while the mean graupel diameter increases (Fig. 3.4k), corresponding to lower mean number concentrations of larger graupel. For hail, the opposite trend occurs, with increasing mean number concentration and mean mixing ratio with increasing ν (Fig. 3.4d, h). The mean hail diameters are small in all simulations until ~4 km, near the freezing level, where the ν10 mean diameter increases significantly (Fig. 3.4*l*). As ν increases, hail grows at the expense of graupel. This is due to a shift in hydrometeor size which transitions graupel into hail. As previously stated, the ν10 simulation is the only simulation to accumulate hail at the surface. Although the mean number of hail particles is small at the surface (Fig. 3.4d), the ν10 mean mixing ratio (Fig. 3.4h) and mean diameter (Fig. 3.4*l*) demonstrate that a few large hail particles do reach the

surface. Because these values are means, it is important to note that hail is not growing in this case, but rather that this trend is indicative of smaller hail stones readily melting and thus leaving a few, large hail stones reaching the surface. These processes will shift the mean hail diameter to larger sizes. To better understand these relationships and differences, we now examine the microphysical process rates.

3.2 Microphysical Process Rates

To understand the rain DSDs at the surface produced by the different cloud types and as a result of specifying ν, we must understand the microphysical processes occurring aloft. An analysis of these process rates will help to explain some of the trends explored above, such as those of the surface precipitation and the hydrometeor characteristics. We have created a rain budget in order to contextualize how each of the microphysical process rates contribute to the population of rain in the column and at the surface. Each microphysical process rate acts as either a source or sink to the overall rain budget and is shown in Figure 3.5. The total amount of rain is also shown in Figure 3.5 and represents the difference between the source and sinks. Details of each process and its categorization as a source or sink were described in Section 2.4.

3.2.1 MS Case - Warm-Phase Microphysics

A budget analysis of the processes contributing to the rain in the MS case shows that cloud water collection between ν1-4 varies by ~10% between the maximum (ν4) and minimum (ν3) (Fig. 3.5a). Additionally, when moving from ν4 to the narrowest distribution, ν10, cloud water collection decreases by ~17%. The peak in cloud water collection occurs in the ν4 simulation, which is the simulation with the largest mean rain number concentration (Fig. 3.4b). An increased number of raindrops yields more opportunities for cloud droplets to be collected by rain drops, which explains the peak in cloud collection in the ν4 simulation.

The sum of the condensation/evaporation terms are negative, thereby indicating that the evaporation of rain is dominant over the growth of rain via condensation in all of the simulations regardless of ν. Condensation/evaporation increases from $\nu 1$ through $\nu 4$ by ~35%. This is due to the increase in concentrations of smaller drops (Fig. 3.4a, i) which evaporate more readily than larger drops. The maximum in evaporation occurs in the $\nu 4$ simulation. Stronger evaporation is associated with areas of smaller mixing ratios, like around the edge of a system (Fig. 3.4e). After the maximum in evaporation occurs in the ν 4 simulation, it decreases by ~15% in the $\nu 10$ simulation. For $\nu 10$, the narrower distribution does not allow for many small drops (Fig 1.1), which are readily evaporated in the $\nu 1$-4 simulations.

These patterns in cloud water collection and evaporation together played a role in the accumulated precipitation at the surface for the MS case. Cloud water collection remains fairly consistent between all simulations, but evaporation increases noticeably between $\nu 1$ and v4. This causes the accumulated precipitation to decrease (Fig. 3.1a, 7a (black bars)). An increase in evaporation with increasing cloud shape parameter was also noted by Igel and van den Heever (2017a-c).

3.2.2 CD Case - Mixed and Ice Phase Microphysics

For the CD case, both warm and ice phase microphysical processes are occurring and interacting. The contributions to the rain budget are shown in Figure 3.5b. Focusing on the warm rain processes first, differences can be seen in cloud water collection, which increases 20% from $\nu 1$ to $\nu 2$, and then decreases by less than 7% for each subsequent increase in ν (Fig. 3.5b). Comparable trends in cloud water collection are also observed in the MS case. Evaporation increases from $\nu 1$ to $\nu 2$ by ~25%, remains consistent from $\nu 2$ through $\nu 4$, and then decreases

17% from $\nu 4$ to $\nu 10$. Between the cloud water collection and condensation/evaporation terms, evaporation is the microphysical processes most influenced by changes in ν.

Now turning our attention to the mixed phase processes, when compared to some of the microphysical process rates examined here that have larger magnitudes, the melting of aggregates and snow do not significantly contribute to the rain budget for any ν value. Similarly, the riming of rain by hail, graupel, snow and aggregates are small sinks in the rain budget and are of similar magnitudes for all ν values. A noticeable trend is, however, visible in the riming of pristine ice, which increases from $\nu 1$ to $\nu 2$ by ~10%, and then decreases ~50% from $\nu 2$ to $\nu 10$. Just above the freezing level, where rain and pristine ice can coexist, pristine ice has a higher number concentration in comparison to any other ice species. Therefore, rain has a greater chance of colliding with pristine ice, which encourages the formation and growth of larger ice species by creating graupel or hail embryos via the freezing of raindrops. Further discussion of the interactions of pristine ice and rain are included below with respect to the formation of hail.

Melting of graupel makes only a small contribution to the generation of rain when compared to some of the other microphysical processes, but nevertheless decreases ~30% from $\nu 1$ to $\nu 2$ and then remains consistent. In Figure 3.4(c,g), $\nu 1$ has the highest mean graupel number concentration and mixing ratio, so there is more graupel available to melt and a higher melting rate. $\nu 2$- $\nu 10$ have more similar mean graupel number concentration and mixing ratio profiles, so similar graupel melting rates are expected.

The most noticeable difference amongst the simulations in the rain sources is in the hail melting categories, including both thermodynamic melting and collisional melting. The melting of hail (Fig. 3.5b) as a source of rain increases by ~530% as the value of ν increases from $\nu 1$ to $\nu 10$. This increase in hail melting also occurs concurrently with a ~100% decrease in collisional

melting as ν increases. The reduced collisional melting allows for increased opportunity for thermodynamic melting. The hail number concentrations and mixing ratios increase with increasing ν, but have smaller mean sizes aloft (Fig. 3.4d,h, *l*), suggesting that the $\nu 10$ simulation has significant amounts of small hail. To better understand these hail melting processes, we now examine them further.

The overall sum of thermodynamic hail melting and collisional melting process rates with height is presented in Figure 3.6. Figure 3.6a shows the summation of collisional melting of hail as a function of height. As ν increases, the peak in collisional melting for $\nu 1$-4 found near 4 km AGL (around the freezing level), decreases, and there is minimal collisional melting in the $\nu 10$ simulation. The opposite trend occurs in thermodynamic hail melting (Fig.3.6b). As ν increases, the peak in thermodynamic hail melting occurring at ~2.5 km AGL increases. This increase in thermodynamic melting is due to several factors. First, as ν increases, both the mean number concentration and mixing ratio of hail increase, so there is more hail mass available to melt (Fig. 3.4d). Second, as ν increases there is a decrease in collisional melting, so there is more hail available to melt thermodynamically (Fig. 3.6a). Below 2 km, almost all of the hail present in $\nu 1$ through $\nu 4$ melts, and so the process rates trend toward zero; however, the $\nu 10$ hail continues to melt all the way through to the surface, with a few, large hail stones making it to the surface in this simulation only (Fig. 3.4h, i).

We now explore these two mechanisms of melting hail, how they vary as a function of ν, and how they lead to hail accumulating at the surface in the $\nu 10$ simulation. As discussed in Section 3.1.1, we found the $\nu 10$ simulation has the largest mean rain number concentration, mixing ratio, and diameter at higher altitudes (6.5-8km) than any of the other simulations (Fig. 3.4 b, f, j). The rain that is present at this height in the atmosphere (6.5-8 km) experiences cold

temperatures, which lowers the internal energy of the rain. Internal energy determines whether a collision between an ice hydrometeor and a rain drop will initiate collisional melting or freezing into an embryo. The rain in the $\nu 10$ simulation has a lower internal energy than in any other simulation at this height because $\nu 1$- $\nu 4$ do not produce rain at these levels. Just below this level, in the mixed-phase region (3.5 – 4.5 km, with the melting level at ~4 km), rain has the potential to interact with other ice species, such as pristine ice. Since the rain in $\nu 10$ has a much lower internal energy, when it collides with other ice species in the mixed phase region, the supercooled rain initiates freezing to form graupel or hail embryos. This contributes to the lack of collisional melting in the $\nu 10$ case (Fig. 3.6a). In the other ν simulations, rain drops have a higher internal energy (warmer temperature) because they originated lower in altitude in the atmosphere. When these higher internal energy rain drops collide with ice hydrometeors, the rain has a high enough internal energy to initiate melting rather than freezing. This interaction between rain drops and ice hydrometeors results in rain which has a lower internal energy just under 4 km AGL (Fig. 3.6c). Another factor that could contribute to decreased collisional melting in the $\nu 10$ case is decreased collisions between rain and hail in the mixed layer. With a narrow distribution of rain, and a large concentration of small-sized hail (Fig. 3.4 d, *l*), fall-speeds may be similar between the two species thereby reducing the collisions. This, in addition to the lower internal energy of rain as discussed above, results in little collisional melting in the $\nu 10$ case.

Since limited collisional melting occurs in the $\nu 10$ simulation, more hail can descend to lower levels where warm (> 0º C) environmental temperatures trigger melting (Fig. 3.6b). There is thus more thermodynamic melting in the $\nu 10$ case, as there is more hail available to melt in this case than in the other cases where much of the hail is lost due to collisional melting. Small

hail particles are quick to melt and rapidly increase the sum of hail that thermodynamically melts (Fig. 3.6b). A few, very large hail particles are falling fast enough and are able to descend through the lower levels to reach the surface before melting (Fig. 3.4*l*). These findings provide evidence that the selection of ν has feedbacks both within the mixed-phase and ice phase aloft.

Though the overall accumulated precipitation is similar in all simulations regardless of ν in the CD case (Fig. 3.1b), the interactions between rain and ice hydrometeors reveal complex feedbacks of changing ν on microphysical processes. Most evidently, as ν increases, melting of hail thermodynamically increases monotonically, while melting of ice hydrometeors via collisions with rain decreases monotonically. These trends in melting processes result in the $\nu 10$ simulation being the only simulation to sustain hail through the atmosphere to the surface.

3.3 Bin Model Results

As previously stated, in a numerical modeling setup which utilizes bin microphysics the *a priori* selection of ν is not necessary. We examined both the MS-BIN and CD-BIN simulations to assess how the predicted shape of the rain drop spectrum evolves in space and time. Using the previously described distribution fitting method (Section 2.2), we estimate the ν values the bin scheme produces. This allows for a comparison between the constrained ν value of the bulk microphysics scheme and the evolving ν values predicted by the bin microphysics scheme.

3.3.1 MS Case

To examine how the vertical structure of the ν varies within the system, four horizontal cross sections at various vertical levels have been selected to analyze the MS case (Fig. 3.7a). At 1.3 km AGL, within the stratocumulus layer described in Section 2.1, a high frequency of ν=5-10 occurs, suggesting that rain distributions close to cloud top are relatively narrow, with the maximum frequency occurring at ν =8. Slightly lower in altitude, at 0.8 km AGL, which lies

within the layer of stratus clouds, similar trends occur, with a maximum occurring at ν=8. At 0.3 km AGL, in the sub-cloud layer, there is an increased frequency of smaller ν (ν =1-4) compared to those found at higher altitudes. Finally, at the surface, the frequency of ν values resembles the frequencies in the 0.3 km level. Additionally, the most frequent occurrences of ν at the surface range from ν=13-20, with frequencies varying by ~8% within this range. At both the surface and the 0.3km level, relatively similar frequencies occur over a wide range of ν (ν =6-18). This shows the vast variability in rain drop size distributions, and therefor ν values within a single storm morphology. Overall, the MS-BIN simulation reveals high frequencies of large ν values (ν =13-20), most of which extend beyond the values tested within this study. It is evident that there is significant variability in ν in the vertical, which is not possible to represent when using the bulk microphysics schemes. To further explore the distribution of ν values through different regions of the clouds in the MS case, we now examine the distribution of ν in both vertical and horizontal cross sections.

A horizontal cross section at the surface of the MS-BIN showing estimated ν values with precipitation contours at (0, 0.01, 0.1, and 1 mm hr^{-1}) is presented in Figure 3.8a. It is evident that there is an increase in precipitation rate corresponding to areas where ν values are lower (broader distributions), while the edges of the system typically have higher ν values (narrower distributions). A vertical cross section was taken through the point of the highest surface precipitation rate and is shown in Figure 3.8b. Similarly, higher values are ν are found around the cloud edges, with lower ν in the precipitation core. When ν is small (broader distribution), there is a greater variability in the sizes of drops, and hence diverse speeds at which the drops fall. This provides opportunities for rain drops to collide and coalesce into larger drops.

Alternatively, on the edges of the system and higher aloft, evaporation will work to narrow the distribution by preferentially removing the smaller drops.

3.3.2 CD Case

An examination of the frequency of ν occurrences within the CD-BIN simulation at various levels in the vertical reveals how ν varies throughout the vertical structure of the system within layers just above the melting layer, just below the melting layer, within a sub-cloud raining portion of the system, and at the surface (Fig. 3.7b). The vertical levels were chosen to encompass distinct areas within the storm structure. At 4.8 km AGL, which is just above the melting level, the maximum frequency occurs at ν=6. Additionally, higher frequencies of larger ν values are present at this vertical level, representing more narrow distributions. At 3.3km AGL, just below the melting layer, the maximum frequency occurs at ν=4. This vertical level has the lowest frequency of large ν values (>ν=16) when compared to the other vertical levels. Below the melting level, the rain DSD will be most heavily influenced by the melting of ice hydrometeors, particularly collisional melting and thermodynamic hail melting (Fig. 3.5b, Fig. 3.6). These two melting processes will generate rain drops with larger sizes thereby acting to broaden the DSDs by adding raindrops to the tail of the size distribution. The 0.7 km level was selected as it is below cloud base and also encompasses an area of the storm where precipitation is falling toward the surface. Here, the maximum frequency occurs at ν=7, which is a higher ν value than the respective maxima in the other vertical levels. This indicates that within the precipitating portion of the system, evaporation and droplet breakup act to narrow the distribution towards drops of a similar size, with evaporation removing small drops and breakup removing large drops. At the surface, the maximum frequency occurs at ν=5 with lower frequencies of large ν values than the 0.7 km layer above. This maximum represents a broader

distribution than at 0.7km, which suggests enhanced collision coalescence or further melting of ice species is acting to broaden the distribution between 0.7 km and just above the surface. We now explore the distribution of ν values through different regions of the CD case through examination of vertical and horizontal cross sections.

A surface view of the estimated ν values in the CD-BIN simulation is presented in Figure 3.8c. Precipitation rate contours (0,1,10,50,100 mm hr^{-1}) have been added to contextualize the calculated ν values in comparison to how heavy the rain is near the surface. The heaviest rainfall rates coincide with areas with the highest ν values, the opposite trend to that observed in the MS-BIN simulation. High ν values are also observed around the edges of the system, similar to the MS-BIN simulation. Lower ν values occur in areas where the rain rate is less than1 mm hr^{-1}. When examining the vertical cross section through the point of maximum precipitation of the left-mover (Fig. 3.8d), the highest ν values occur in the core of the system with ν decreasing outwards until the edges, where high ν values occur again. As was shown by Saleeby et al. (2021), aggressive drop breakup can force drops towards an equilibrium size. This is quite likely to be the case in this precipitation core where many drops are available and are colliding and coalescing towards sufficient sizes to begin to breakup. This is facilitated in part by the turbulent motions in such storms. Such processes would result in a continually narrowing spectrum as drop breakup forces drops to an equilibrium size. Moving outwards from the core in both directions, lower ν values begin to occur within the more stratiform region of the CD system. Here, where there are lower precipitation rates, fewer drops are available for collision and coalescence to generate drops large enough to trigger breakup. Less droplet breakup will allow rain DSDs to remain broader. Additionally, in areas with lower ν that are reach high enough aloft to sustain ice

species, we would expect enhanced collisional melting which would further act to broaden the rain DSD (Fig. 3.5).

Interestingly, the vertical cross sections in both cases show converse patterns. In the moist, dynamic CD case, higher precipitation rates towards the core of the system correspond with higher ν values, which we speculate are due to aggressive drop breakup, facilitated by the turbulent motions within such systems. In the weaker, less dynamic MS case, higher precipitation rates correspond to lower ν values. This further shows how different storm morphologies are shaped by different microphysical processes, and how these processes influence the rain DSDs and subsequently, ν. Additionally, this analysis demonstrates the constraints imposed by applying a single *a priori* ν in a two-moment bulk microphysics scheme. In both cases, the ν values within the bin scheme frequently spanned values ranging from 0 to 20 and showed variations both spatially and temporally.

3.4 Comparison with Observations

In order to ensure that the atmospheric phenomena modeled by numerical simulations accurately represent the phenomena that occur in nature, comparison to atmospheric observations is essential. This remains challenging due to the spatial and temporal sampling differences between models and observations. We employ a previously developed model-disdrometer inter-comparison framework in order to compare the model simulations of focus to a global disdrometer data set previously examined in D18 and Dolan et al. (2021). Figure 3.9 shows the conceptual framework of between the log of the intercept parameter ($\log N_w$) and median drop diameter (D_0) phase space. In this methodology, examining the frequency of points at the surface in $\log N_w$ – D_0 space provides context for how well the model is able to capture the natural variability of rain as revealed by the disdrometer observations. In the 2D phase space of $\log N_w$ –

D_0, higher $\log N_w$ with smaller D_0 represents a population of hydrometeors which is large in number, but is comprised of smaller drop sizes (Figure 3.9). Conversely, a small $\log N_w$ and large D_0 represents a population with larger drop sizes, but a smaller number of drops. D18 and Figure 3.9 show a conceptual model where areas of higher $\log N_w$ with smaller D_0 may indicate weaker convection and the dominance of collision-coalescence microphysical processes. Additionally, areas with low $\log N_w$ and large D_0 may indicate rain formed via ice-based processes. In between these extremes, are areas where vapor deposition and aggregation/riming fill the 2D phase space.

3.4.1 MS Case

For reference to an observational case which is similar to the MS case, Figure 3.10 a-f shows an outline for observations collected in the Eastern North Atlantic (ENA). A DOE Atmospheric Radiation Measurement (ARM) disdrometer was placed on Graciosa Island in the Azores from October 2014 – January 2018 (Wang and Bartholomew 2014, Wang et al. 2021). We note here that these observations include the spectrum of precipitation experienced over a mid-Atlantic oceanic site over all seasons, and therefore we do not expect the MS results to exactly match the observations. However, we use the disdrometer data as a guide to illustrate the bounds of $\log N_w$ and D_0 values observed in nature in an environment encompassing the MS case. In the spirit of comparing models and observations, as discussed further by Dolan et al. (2021), we do note that disdrometers are limited in their detection of small drops, and may therefore underestimate the frequency of points in the high $\log N_w$, small D_0 regime. Additionally, the infrequent nature of large drops may also lead to them being under sampled by disdrometers, and therefore areas of low $\log N_w$ and large D_0 may also be underestimated. However, these comparisons are nevertheless insightful in determining the representativeness of numerical models.

In the MS case, all frequencies occur within the high $\log N_w$ small D_0 portion of the phase space (Fig. 3.10 a-f), which is consistent with the overall characteristics of the MS case in which there is a larger number of smaller drops, as shown above (Figure 3.4 a,i). As the value of ν increases in the bulk simulations, the frequency of points moves to higher $\log N_w$ and even smaller D_0 within the phase space. Using the ENA observational outline as a guide for comparison, the results of the surface $\log N_w$ and D_0 values from $\nu 1$ and $\nu 2$ simulations occupy the most similar space to those of the observations. While $\nu 2$ is completely within the bounds of the observations, $\nu 1$ overlaps with the observational outline, but extends into higher $\log N_w$ values. However, as ν increases from 3 through to 10, the simulations deviate significantly from the disdrometer observations, moving towards larger $\log N_w$ and smaller D_0. For the MS case, the smaller ν values therefore coincide more closely with surface observations of similar environmental conditions. However, it is important to remember that the sampling capabilities of a ground based disdrometer are limited in high $\log N_w$ and low D_0. For the bin simulation (Figure 3.4f), the frequencies of the model simulations align well with the observational guideline. In this scenario, the bin simulation aligns more closely with the observational guideline in comparison to the bulk microphysics simulations. Additionally, within this observational data set we use to guide our analysis, deeper oceanic convective systems in addition to many shallow maritime cloud systems were sampled, not just cumulus under stratocumulus like what is present in the model simulation.

3.4.2 CD Case

The black outline on Figure 3.10 g-l represents the $\log N_w$-D_0 for disdrometer observations taken during the Mid-latitude Continental Clouds and Convection Experiment (MC3E) field campaign (Petersen et al. 2011, Jensen et al. 2015). In this case, 5 disdrometers

were deployed from April-June 2011 in north central Oklahoma. These observations encompass environments and storm systems similar to the CD case, and therefore provide a guide for analyzing $\log N_w$-D_0 found in isolated mid-latitude convection. Again, we note that sampling within deep convective cores can be limited when compared to sampling in other, larger regions of stratiform using a disdrometer.

The CD case occupies a much larger breadth of the 2D phase space (Fig. 3.10 g- *l*) compared to the MS case (Fig. 3.10 a-f). This is to be expected as convective storm morphologies, such as represented by the CD case, have many different precipitation generation mechanisms throughout the storm lifecycle, including trailing stratiform with light rain to heavy precipitation within the convective core. For smaller ν, there is a high frequency of moderate $\log N_w$ (4-6) and small D_0 (~1 mm) as shown by the warmer colors (Figs 3.10g,h). As the value of ν increases, the frequency at moderate $\log N_w$ and small D_0 decreases (Figs. 3.11i-j), which acts to widen the breadth of the simulated $\log N_w$ and D_0 values. Additionally, for larger ν, the tail of low frequencies extending into large D_0 approaching 4 mm begins to truncate when compared with the smaller ν. Overall, increasing ν broadens the spectra of $\log N_w$-D_0 values at the expense of the large drop sizes and the high concentrations of 1 mm-sized drops. As ν increases, the distribution narrows, so there is less droplet collision and coalescence to grow drops to larger sizes. Large drop sizes are also less frequent as ν increases because more hail is reaching the surface, rather than melting to form large rain drops. In the bin simulation (Fig. 3.10 *l*), the tail towards larger D_0 is also truncated, similar to trends in larger ν values in the bulk simulations. The breadth of frequencies reaching towards moderate $\log N_w$ and D_0 is significantly reduced, similar to lower νvalues.

All of the ν sensitivity tests overlap with the observational bounds. However, all ν values in the CD bulk microphysics cases have a longer tail of frequencies extending into larger D_0 and low $\log N_w$ compared to the observations. This corresponds to a few, large drops occurring within the model simulations which appear to be outside of the disdrometer observed ranges. Frequencies in this area are very low in all simulations. These may not be able to be measured by disdrometeors given the compact nature of convective cores which decreases the likelihood that such convective cores pass within the catchment area of the disdrometer. Additionally, the area of highest frequency within the simulations, at high $\log N_w$ and D_0 ~1 mm, does not occur within the observations (not shown herein, see Saleeby et al. 2021). This is due to the drop breakup parameterization that generates a high frequency of drops with ~ 1.0 mm equilibrium diameter (Saleeby et al. 2021). As the value of ν increases, the model simulations begin to fully occupy the space in moderate $\log N_w$ (between 2.5-3) and moderate D_0 (1.5-2.5 mm). This region represents an area with moderate numbers of drops that are of a moderate size. As the distribution narrows, collision and coalescence decreases, limiting the ability of drops to grow to large sizes and therefore remain a more moderate size. In general, all of the CD ν cases cover the variations measured in the MC3E observations, however, the simulations do extend into areas with a large number of small drops and areas with a small number of large drops. And importantly, increasing ν broadens the simulation $\log N_w - D_0$ spectrum and reduces the high frequency of points around $D_0 = 1$ mm.

This multi-parameter framework allows for comparison between models and observations to assess whether the models are generally capture the number and size of drops that occur in the natural world. In the MS case, lower ν values correspond more closely with the observations of a similar storm type. In contrast, higher ν values in the CD extend far enough

into moderate numbers of moderate sized drops in order to encompass the variation measured in observations. It is important to note we explored some important microphysical changes in the $\nu 10$ simulation, including hail accumulating at the surface, which were not present in the other simulations. Microphysical processes such as droplet breakup and collision coalescence influence the ability for the drop size distribution to broaden. These results further emphasize the need to strategically select the value of ν. This coincides with the bin microphysics simulations, where the value of ν changes in the horizontal, vertical, and over the course of an entire simulation. Together, the bin microphysics simulations and comparisons with observations show that appropriate ν values may depend on the storm type of focus, and hence assigning one general value for all model simulations is challenging.

FIGURES

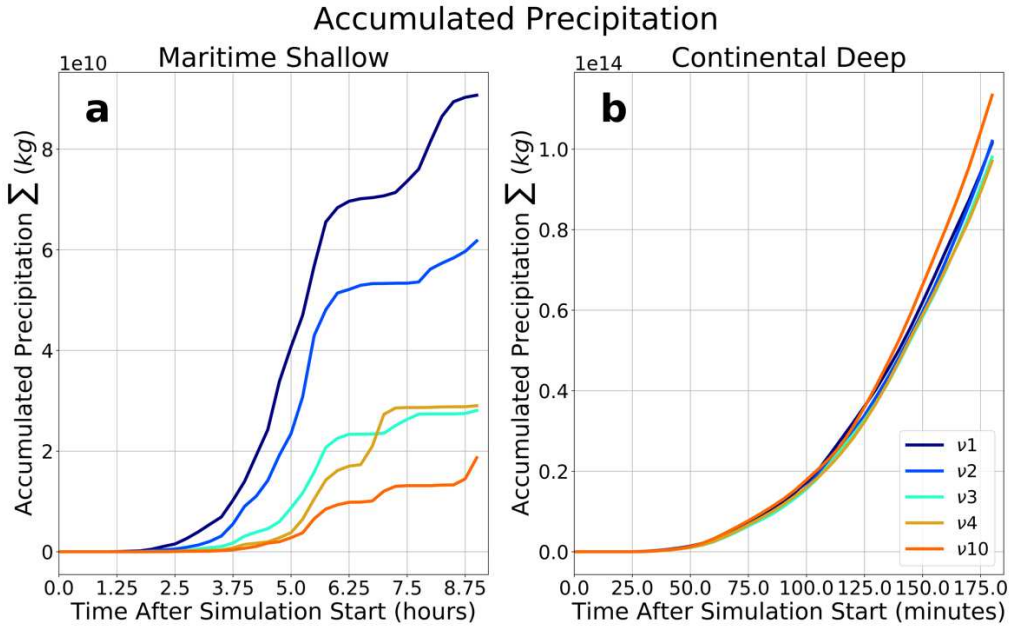

Figure 3.1: Time series of domain-integrated accumulated surface precipitation for (a) the MS case and (b) the CD case.

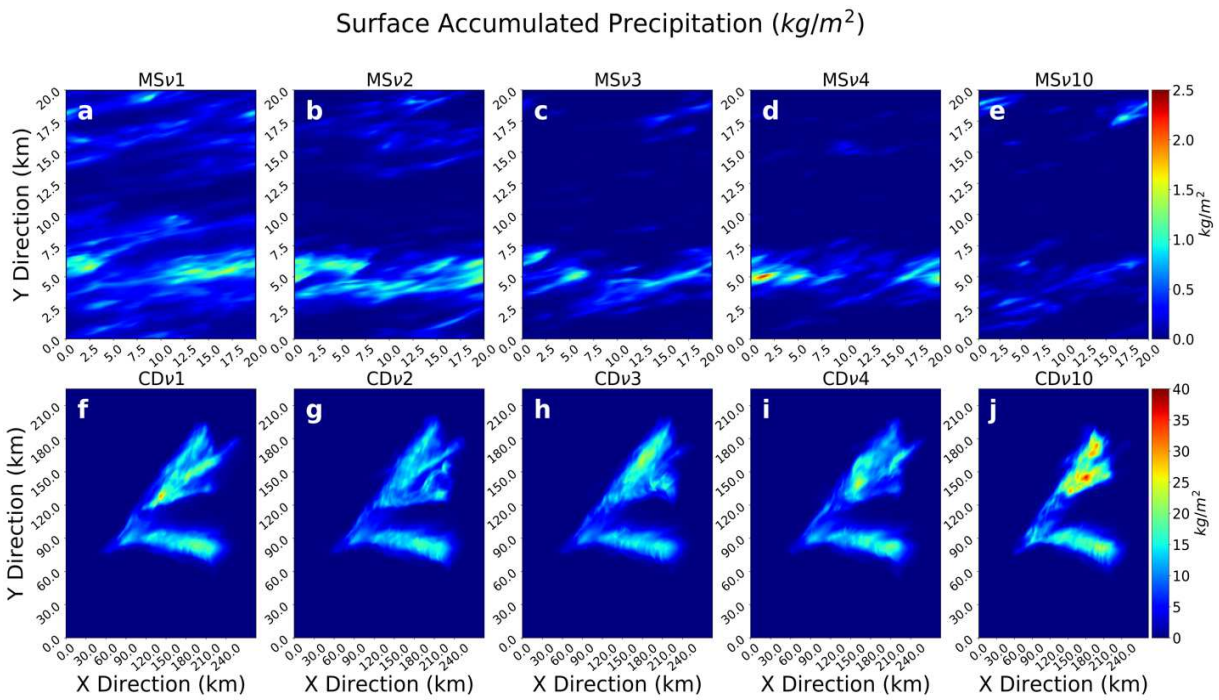

Figure 3.2: The distribution of surface accumulated precipitation over the duration of the simulation in (kg/m^2) as a function of ν for the (top row) MS case and (bottom row) the CD case.

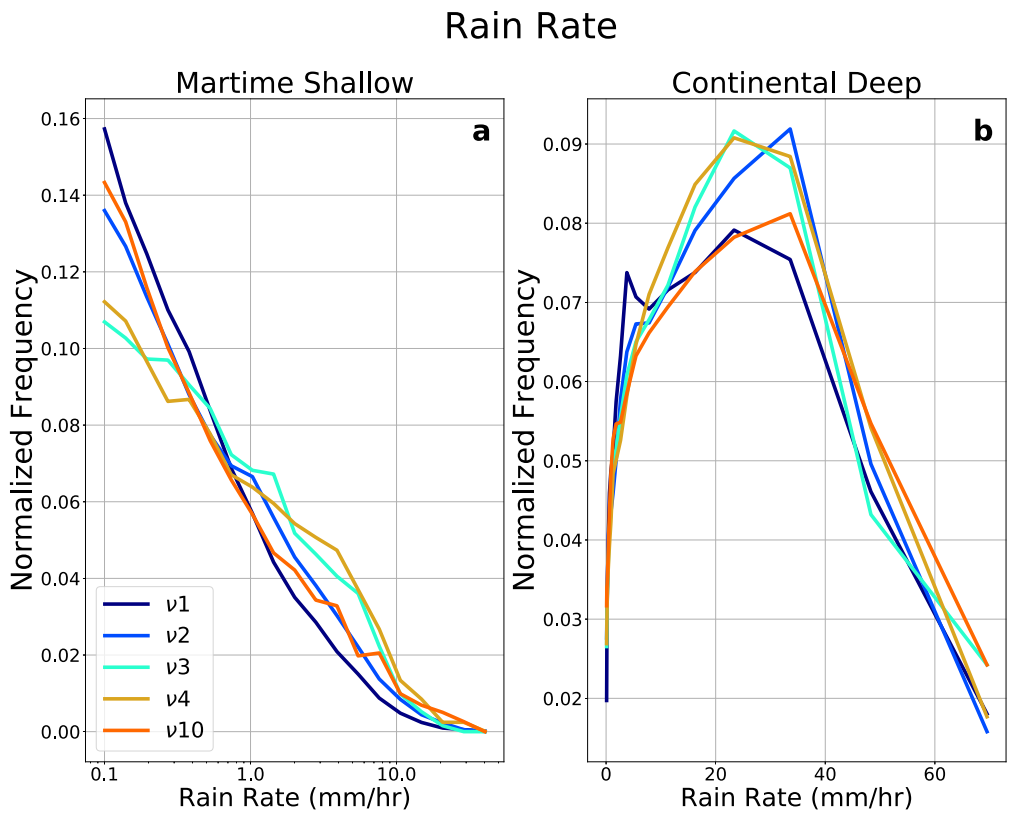

Figure 3.3: a) Histogram of MS case and b) CD case rain rates (mm hr^{-1}) in rainy columns (vertically integrated rain a) >0.01 mm b) > 0.1 mm). The histograms are calculated as a normalized frequency with log bin widths.

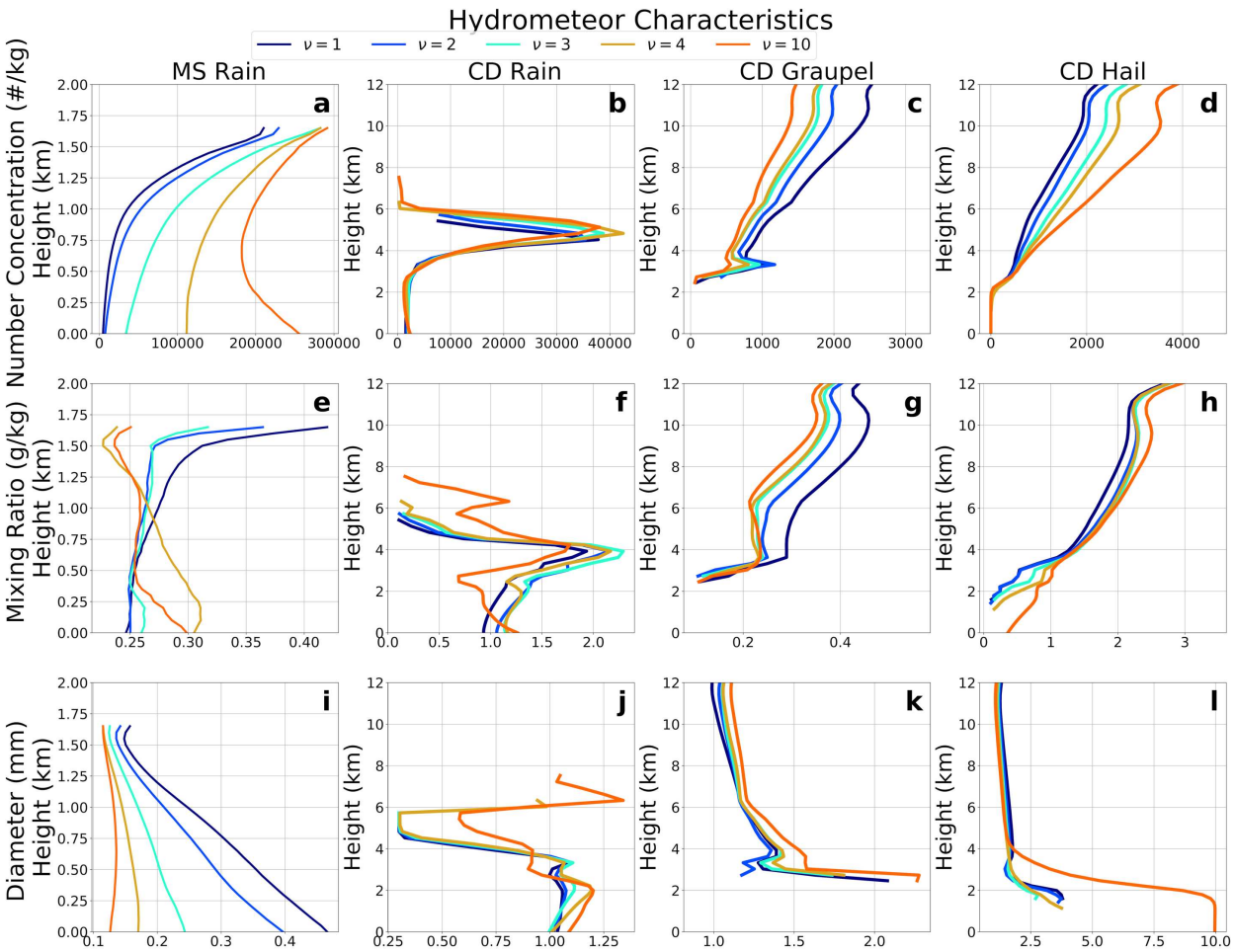

Figure 3.4: (a-d) Mean hydrometeor number concentration (# /kg),(e-h) mixing ratio (g/kg) , and (i-*l*) diameter (mm) as a function of height for (left column) rain in the MS case, (2^{nd}-4^{th} columns) rain, graupel and hail for the CD case. Only points with corresponding mixing ratio greater than 0.1 g/kg are included in the calculation of the mean.

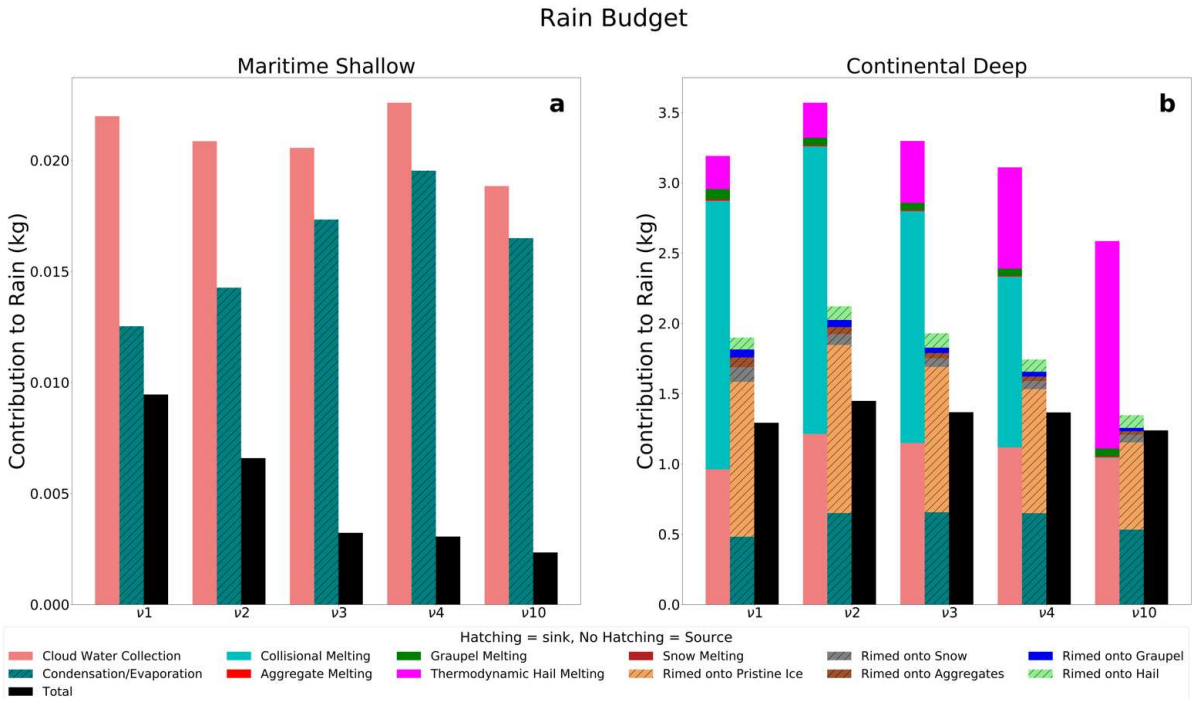

Figure 3.5: Rain budget (kg) for the a) MS and b) CD case with the sources of rain in the unhatched bars, the sinks of rain represented using the hatched bars, and the total (source – sink) in black. Note that while the sources and sinks are all plotted using the same axes, the sink terms are negative contributions to the budget. Each of the processes shown here are explained in the text. Only cloud water collection and condensation/evaporation are shown for a) as this is a warm rain case.

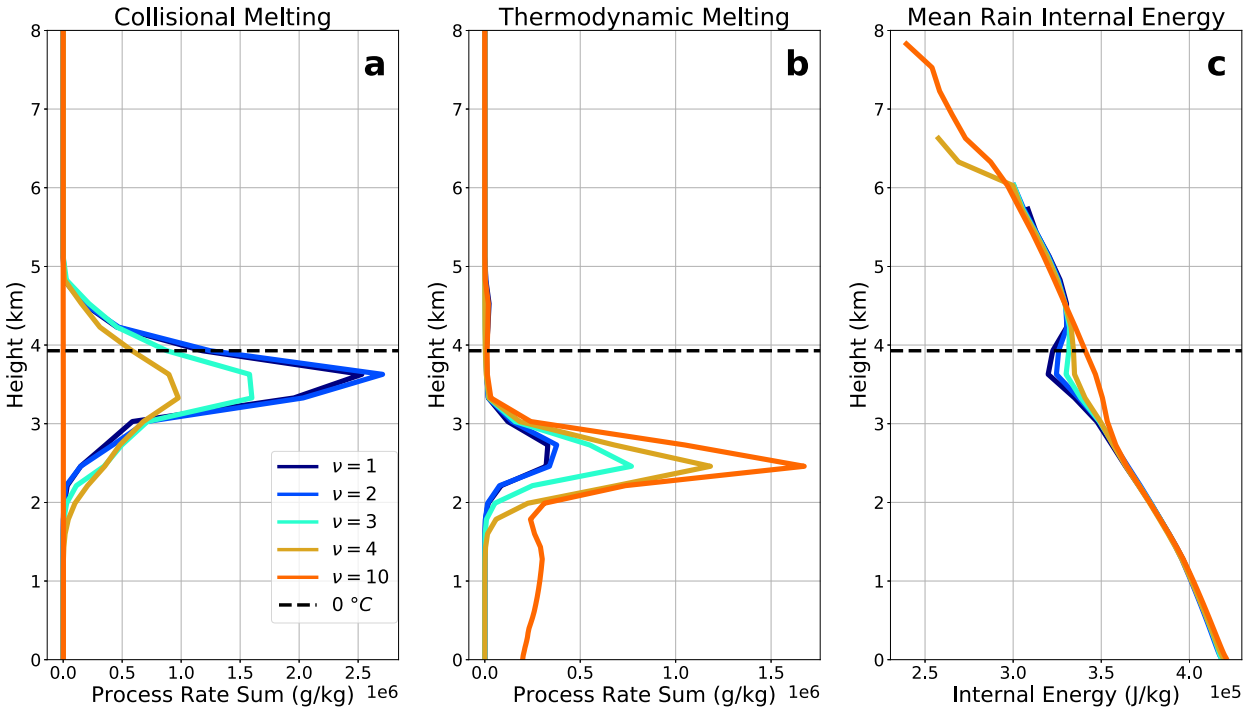

Figure 3.6: Horizontally and temporally integrated profiles of hail removed from the hail category by (a) collisional melting through a collision with a liquid hydrometeor, and (b) by thermodynamic melting. (c) represents the horizontal and temporal mean of the rain internal energy (see text for explanation). Black dashed line denotes the 0°C level.

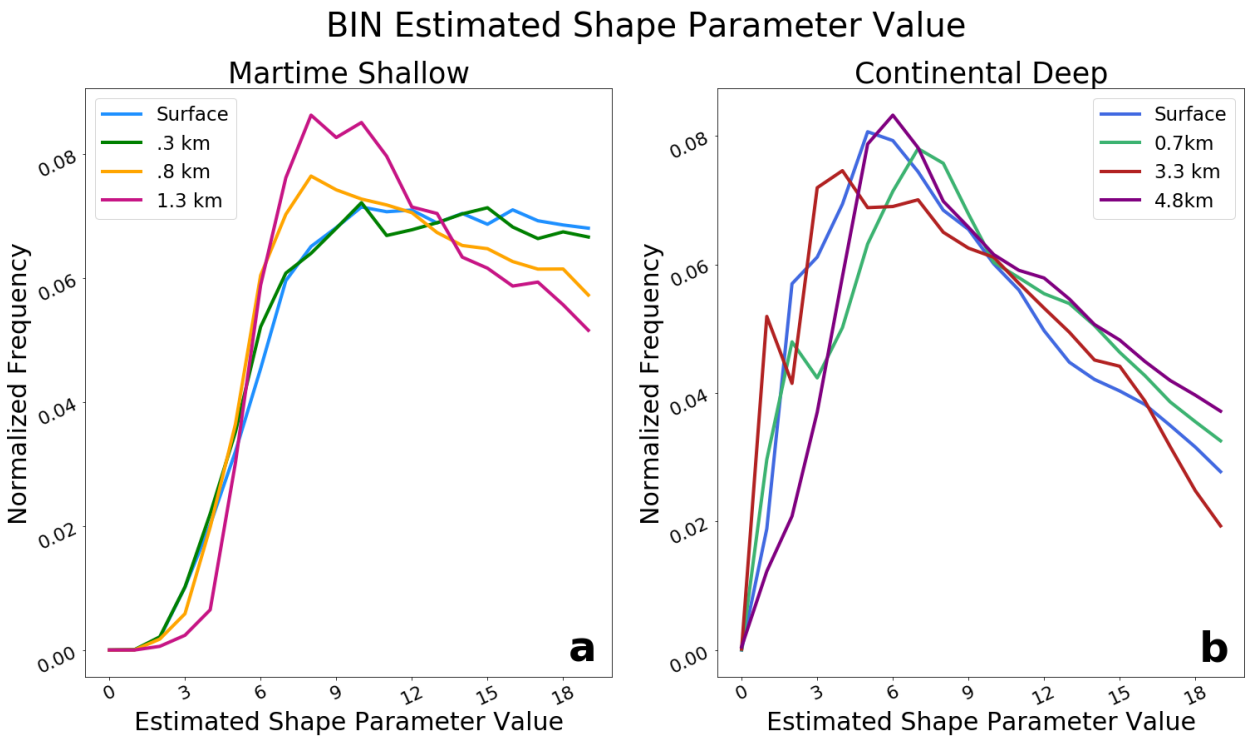

Figure 3.7: (a) Normalized frequency distributions of the rain shape parameter value at the surface, 0.3km AGL in a precipitating, sub cloud layer, 0.8km AGL within the stratus layer, and 1.3km AGL within the stratocumulus layer for the MS case; (b) same as in (a) but for the CD case and vertical levels: the surface, 0.7 km AGL in the sub cloud layer, 3.3 km which is in cloud just below the melting level, and 4.8 km which is in cloud above the melting level.

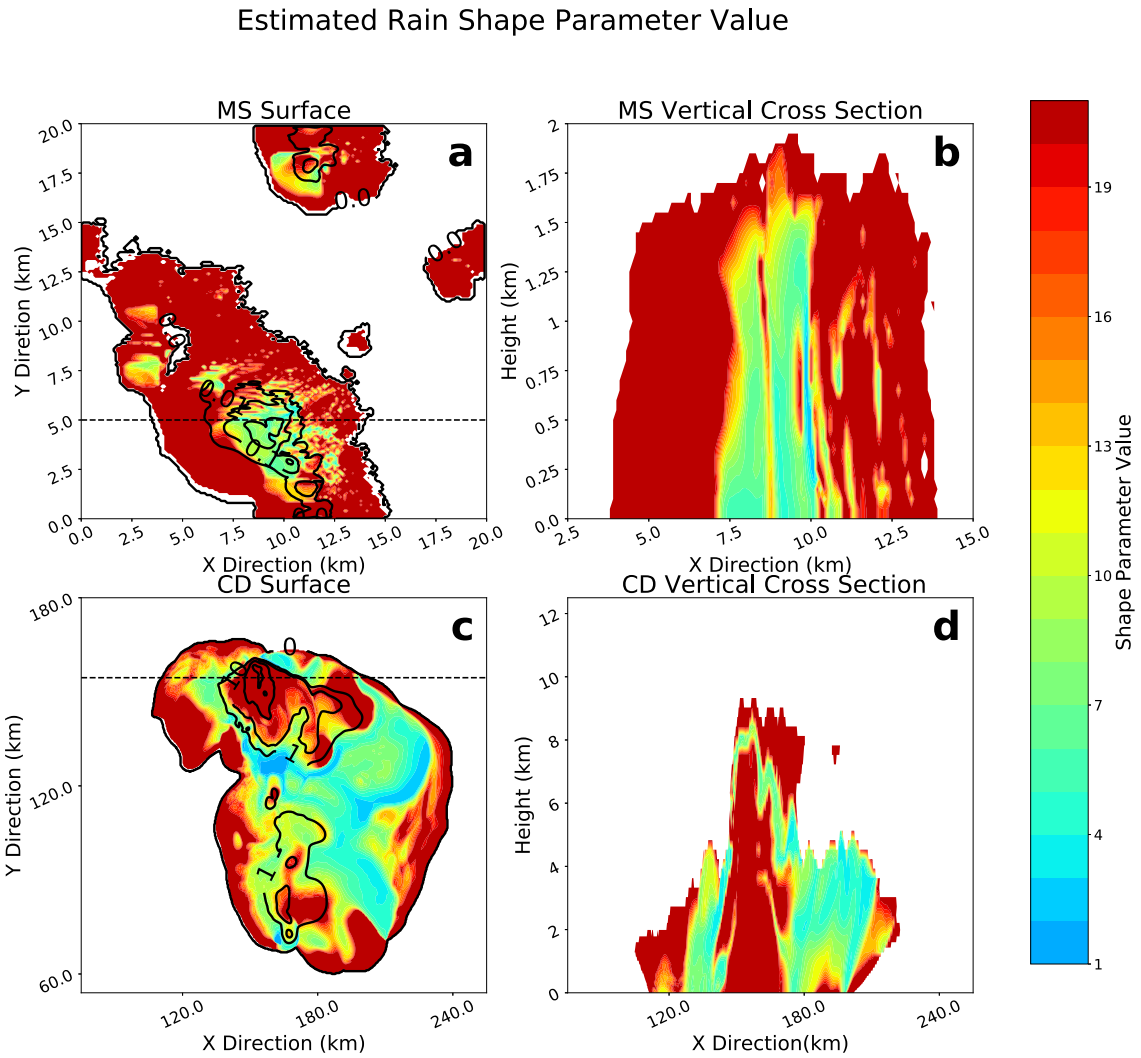

Figure 3.8: (a) A horizontal cross section at the surface for the MS-BIN case with estimated rain shape parameter values in the filled contours. MS surface precipitation rates are contoured in black with levels of (0,0.01, 0.1, 1 mm hr^{-1}) in (a), and black dashed line represents the location of the vertical cross section in (b). (c) Same as in (a) but for the CD case with precipitation rate contour levels of (0,1,10,50,100 mm hr^{-1}), and black dashed line represents the location of the vertical cross section in (d).

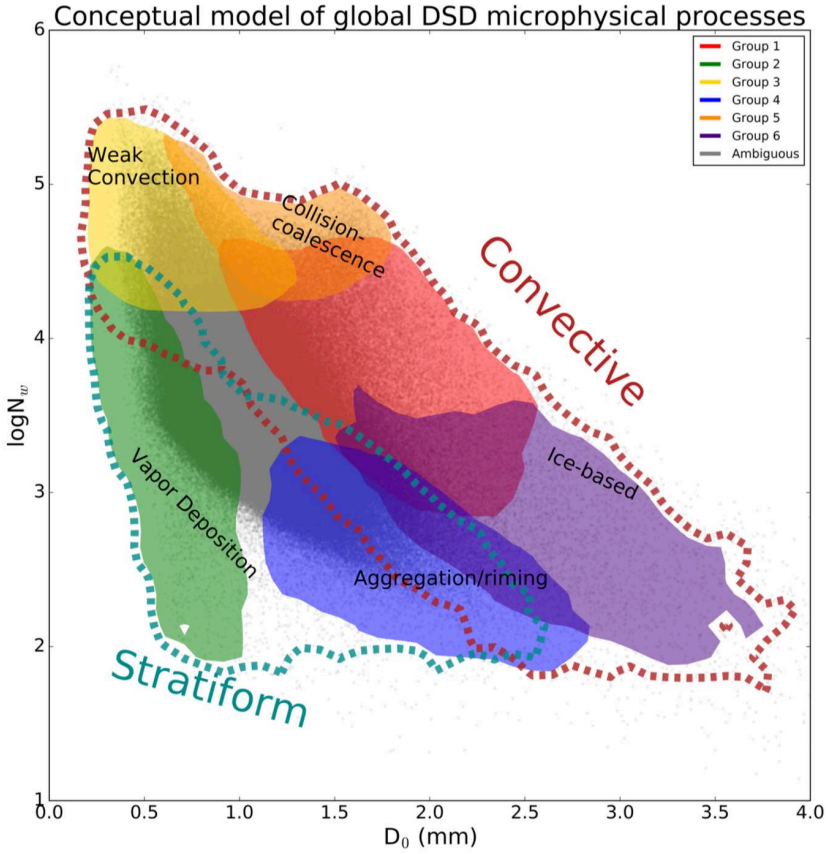

Figure 3.9: Conceptual model from Dolan et al. 2018 for the 2D model-disdrometer inter-comparison framework. Each group is labeled with the hypothesized dominant microphysical processes involved in creating the surface DSD.

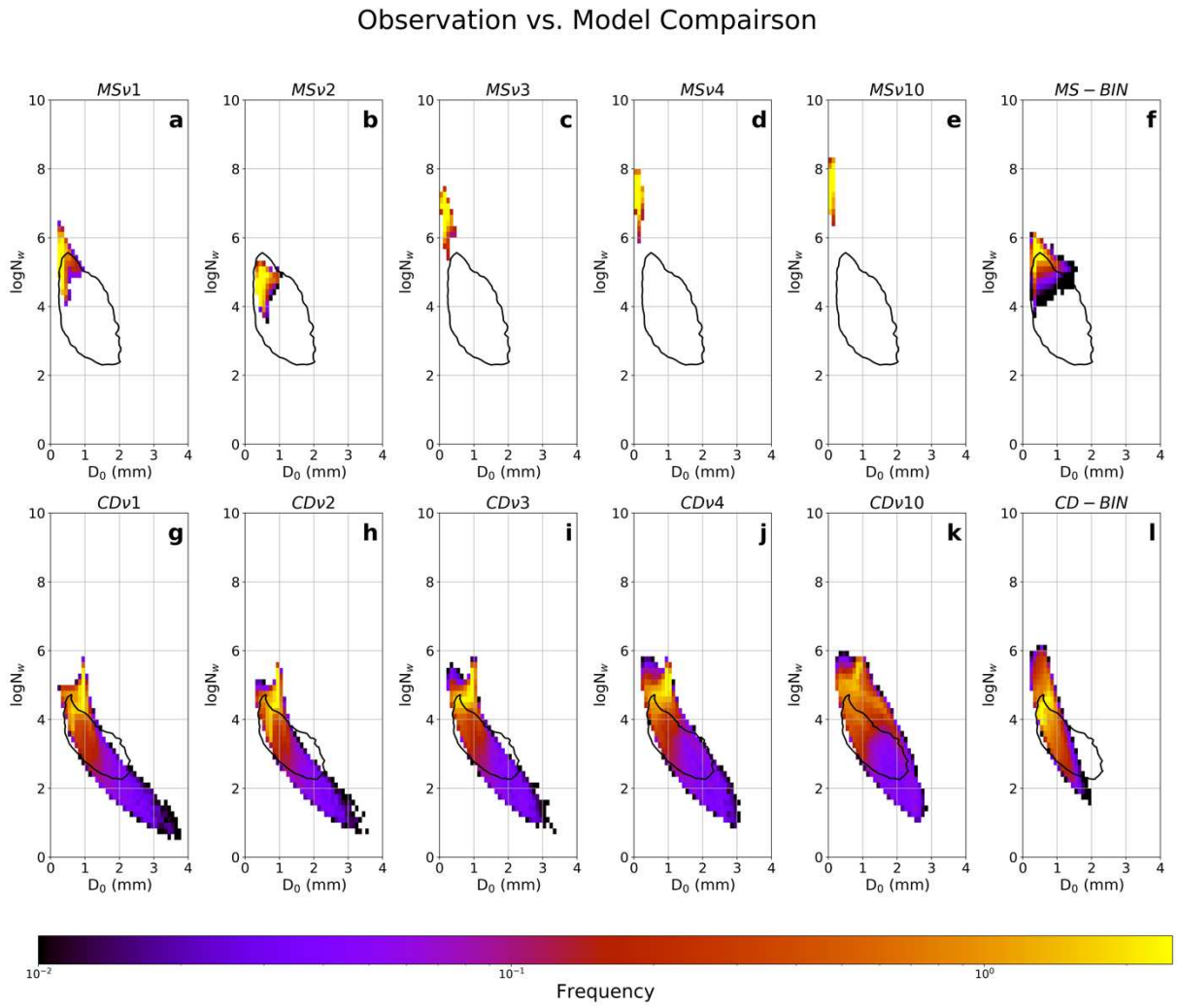

Figure 3.10: (a-e). The contour density plot of surface $LogN_w$ vs. D_0 for the bulk simulations of the MS case, as a function of ν (shaded contours). (f) same as in (a-e) but for the bin simulation. Observational outline shown in black for the ENA site which most closely resembles the environment of the MS case. (g-k) same as in (a-l), but for the CD case and observational outline of the MC3E, which encompasses environments similar to the CD case. See the text for descriptions of the ENA and MC3E cases.

CHAPTER 4 CONCLUSION

4.1 Conclusion

In this study, we examined the sensitivity of microphysical processes and surface precipitation to the *a priori* selection of the rain shape parameter, ν. To encompass a range of possible storm morphologies, we examined a maritime shallow stratocumulus event, representing warm rain only scenarios, and continental deep convection, capturing the complexities of mixed- and ice phase microphysics. We conclude that the sensitivity of precipitation to ν, both aloft and at the surface, and the processes that form the precipitation, are highly dependent on the storm morphology of focus.

In the MS case, ν strongly influences precipitation by shifting the balance between cloud water collection and evaporation as sources and sinks, respectively, to the overall rain budget (Fig. 3.5a). As ν increases, cloud water collection remains relatively constant, while evaporation increases. The balance between these two terms determines the total amount of precipitation at the surface, which was found to decrease as the value of ν increases (Fig. 3.1a). This reduction is due to the increasing influence of evaporation as the drop spectrum narrows.

In the CD case, although changing ν did not result in significant changes to the overall accumulated precipitation, it did impact the microphysical processes forming rain and demonstrated links between the rain and ice-phase microphysics. Collisional melting of hail decreases as ν increases, and is near zero in the ν10 simulation (Fig. 3.6a). This is due to rain being present higher aloft in the ν10 simulation (Fig. 3.4b,f,j), caused by more similarly sized rain drops being lofted more easily than the larger drops of broader size distributions. Rain higher aloft has a lower internal energy (3.6c), and upon collisions with ice hydrometeors, does

not have a sufficiently high internal energy to initiate melting. More hail is then able to reach lower in the atmosphere, where it undergoes thermodynamic melting, which is shown to increase with increasing ν (Fig.3.6b). The feedbacks between rain internal energy, collisional melting, and thermodynamic melting allow for hail to reach the surface in the $\nu 10$ simulation, which is unique when compared to the other simulations.

When ν is not constrained to a single value, such as in bin microphysics schemes where ν evolves in space and time, a variety of rain drop size distributions occur. In the MS-BIN case, high values of ν, corresponding with narrower size distributions, occur around the edges of the convection, while the heavier precipitation cores are characterized by smaller ν values, indicative of broader distributions. In the CD-BIN case, areas with higher rain rates tend toward higher ν. In the vertical, the core of the CD cell had large ν values, with decreasing ν values flanking the convective core, but high ν along the cloud edges. We hypothesize the values near the core are due to droplet breakup, and the values near the edges are influenced by evaporation and entrainment, both of which result in a narrowing of the distribution. Between both cases, it is evident that a single value of ν does not encompass the possible spatiotemporal variability of either morphology, or the variability within the 3D structure and evolution of a single morphology.

Comparison between model simulations and observations ensures natural phenomena are appropriately simulated, while also filling in the sampling gaps of observations, and providing insights into the processes responsible for the observed states. Using the 2D phase space of $\log N_w$ and D_0 and observations from environments similar to the model simulation cases for reference, we found in the MS case, that smaller ν (v=1,2) values more closely aligned with the observational reference. In the CD case, the opposite occurred: larger ν values were better

aligned with the observations in the 2D phase space. These contrasting conclusions further emphasizes that selecting a single *a priori* value for ν may not fully encompass the possible ν values for different storm types, and that such values need to be carefully considered depending on the storm morphology of interest. The bin microphysics simulation of the MS case aligns most closely with the observational guide compared to the bulk microphysics simulations, while the opposite is true for the CD case. This shows that there is also significant variation of different environments even when ν freely evolves throughout a simulation.

Evaluating a range of ν values in different storm types in a bulk microphysics scheme reveals sensitivities of precipitation at the surface and aloft, as well as feedbacks to warm, mixed phase, and ice microphysical properties. Evaluating these same storm systems in a bin microphysics scheme provides understanding of the variability of unconstrained ν values. Comparison with observations provides context to proper selection of *a priori* ν when it is required. Together, these three assessments provide insights towards improving modeling and understanding of precipitation.

4.2 Future Work

It is well understood that microphysics and dynamics are tightly intertwined, where both provide feedbacks to one another. Initial analysis of the dynamic sensitivities to changes in ν as part of this study was inconclusive, but more in-depth analysis would possibly provide meaningful insight into the links between dynamics and microphysics. Additionally, examination of the sensitivity of precipitation and microphysical process to changes in the shape parameter for other hydrometeor species would also be impactful. Igel et al. 2017a,b examined the sensitivity of shallow cumulus clouds to changes in the cloud distribution shape parameter. We

speculate, given the intriguing influences ν has on hail processes, that sensitivity tests involving the hail distribution shape parameter would also prove perspicacious.

REFERENCES

Albrecht, B. A. (1979). A Model of the Thermodynamic Structure of the Trade-Wind Boundary Layer: Part II. Applications. *Journal of the Atmospheric Sciences*, *36*(1), 90–98. https://doi.org/10.1175/1520-0469(1979)036<0090:AMOTTS>2.0.CO;2

Augstein, E., Riehl, H., Ostapoff, F., & Wagner, V. (1973). Mass and Energy Transports in an Undisturbed Atlantic Trade-Wind Flow. *Monthly Weather Review*, *101*(2), 101–111. https://doi.org/10.1175/1520-0493(1973)101<0101:maetia>2.3.co;2

Augstein, E., Schmidt, H., & Ostapoff, F. (1974). The vertical structure of the atmospheric planetary boundary layer in undisturbed trade winds over the Atlantic Ocean. *Boundary-Layer Meteorology*, *6*(1–2), 129–150. https://doi.org/10.1007/BF00232480

Barth, M. C., Kim, S. W., Wang, C., Pickering, K. E., Ott, L. E., Stenchikov, G., … Telenta, B. (2007). Cloud-scale model intercomparison of chemical constituent transport in deep convection. *Atmospheric Chemistry and Physics*, *7*(18), 4709–4731. https://doi.org/10.5194/acp-7-4709-2007

Bringi, V. N., Chandrasekar, V., Hubbert, J., Gorgucci, E., Randeu, W. L., & Schoenhuber, M. (2003). Raindrop size distribution in different climatic regimes from disdrometer and dual-polarized radar analysis. *Journal of the Atmospheric Sciences*, *60*(2), 354–365. https://doi.org/10.1175/1520-0469(2003)060<0354:RSDIDC>2.0.CO;2

Brümmer, B., Augstein, E., & Riehl, H. (1974). On the low-level wind structure in the Atlantic trade. *Quarterly Journal of the Royal Meteorological Society*, *100*(423), 109–121. https://doi.org/10.1002/qj.49710042310

Castro, C. L. (2005). Dynamical downscaling: Assessment of value retained and added using the Regional Atmospheric Modeling System (RAMS). *Journal of Geophysical Research*, *110*(D5), D05108. https://doi.org/10.1029/2004JD004721

Castro, C. L., Pielke, R. A., Adegoke, J. O., Schubert, S. D., & Pegion, P. J. (2007). Investigation of the Summer Climate of the Contiguous United States and Mexico Using the Regional Atmospheric Modeling System (RAMS). Part II: Model Climate Variability. *Journal of Climate*, *20*(15), 3866–3887. https://doi.org/10.1175/JCLI4212.1

Cotton, W. R., Pielke, R. A., Walko, R. L., Liston, G. E., Tremback, C. J., Jiang, H., … McFadden, J. P. (2003). RAMS 2001: Current status and future directions. *Meteorology and Atmospheric Physics*, *82*(1–4), 5–29. https://doi.org/10.1007/s00703-001-0584-9

Dai, A. (2011). Drought under global warming: a review. *WIREs Climate Change*, *2*(1), 45–65. https://doi.org/10.1002/wcc.81

Dolan, B., Fuchs, B., Rutledge, S. A., Barnes, E. A., & Thompson, E. J. (2018). Primary modes of global drop-size distributions. *Journal of the Atmospheric Sciences*, *75*(5), 1453–1476. https://doi.org/10.1175/jas-d-17-0242.1

Dolan, B., Saleeby, S., Rutledge S., van den Heever S., Van Valkeburg K. (2021). A synergistic framework for exploring rain microphyics within observations and models. *J. Geophys. Res.* In Preparation.

Falk, N. M., Igel, A. L., & Igel, M. R. (2019). The relative impact of ice fall speeds and microphysics parameterization complexity on supercell evolution. *Monthly Weather Review*, *147*(7), 2403–2415. https://doi.org/10.1175/MWR-D-18-0417.1

Federico, S., Avolio, E., Petracca, M., Panegrossi, G., Sanò, P., Casella, D., & Dietrich, S. (2014). Simulating lightning into the RAMS model: implementation and preliminary results. *Natural Hazards and Earth System Sciences*, *14*(11), 2933–2950. https://doi.org/10.5194/nhess-14-2933-2014

Ferrier, B. S. (1994). A Double-Moment Multiple-Phase Four-Class Bulk Ice Scheme. Part I: Description. *Journal of the Atmospheric Sciences*, *51*(2), 249–280. https://doi.org/10.1175/1520-0469(1994)051<0249:ADMMPF>2.0.CO;2

Freeman, S. W., Igel, A. L., & van den Heever, S. C. (2019). Relative Sensitivities of Simulated Rainfall to Fixed Shape Parameters and Collection Efficiencies. *Quarterly Journal of the Royal Meteorological Society*, qj.3550. https://doi.org/10.1002/qj.3550

Friedrich, K., Kalina, E. A., Aikins, J., Steiner, M., Gochis, D., Kucera, P. A., Ikeda, K., & Sun, J. (2016). Raindrop Size Distribution and Rain Characteristics during the 2013 Great Colorado Flood. *Journal of Hydrometeorology*, *17*(1), 53–72. https://doi.org/10.1175/JHM-D-14-0184.1

Friedrich, K., Kalina, E. A., Aikins, J., Gochis, D., & Rasmussen, R. (2016). Precipitation and Cloud Structures of Intense Rain during the 2013 Great Colorado Flood. *Journal of Hydrometeorology*, *17*(1), 27–52. https://doi.org/10.1175/JHM-D-14-0157.1

Gilmore, M. S., Straka, J. M., & Rasmussen, E. N. (2004). Precipitation uncertainty due to variations in precipitation particle parameters within a simple microphysics scheme. *Monthly Weather Review*, *132*(11), 2610–2627. https://doi.org/10.1175/MWR2810.1

Grabowski, W. W. (1998). Toward Cloud Resolving Modeling of Large-Scale Tropical Circulations: A Simple Cloud Microphysics Parameterization. *Journal of the Atmospheric Sciences*, *55*(21), 3283–3298. https://doi.org/10.1175/1520-0469(1998)055<3283:TCRMOL>2.0.CO;2

Grant, L. D., & van den Heever, S. C. (2014). Microphysical and Dynamical Characteristics of Low-Precipitation and Classic Supercells. *Journal of the Atmospheric Sciences*, *71*(7), 2604–2624. https://doi.org/10.1175/JAS-D-13-0261.1

Hardin, J., & Guy, N. (2017, December). PyDSD, doi: http://doi.org/10.5281/zenodo.9991

Hopper, L. J., Schumacher, C., Humes, K., & Funk, A. (2019). Drop-Size Distribution Variations Associated with Different Storm Types in Southeast Texas. *Atmosphere*, *11*(1), 8. https://doi.org/10.3390/atmos11010008

Hosannah, N., Parsiani, H., & González, J. E. (2015). The role of aerosols in convective processes during the midsummer drought in the Caribbean. *Advances in Meteorology*, *2015*(July). https://doi.org/10.1155/2015/261239

Igel, A. L., & van den Heever, S. C. (2017a). The importance of the shape of cloud droplet size distributions in shallow cumulus clouds. Part II: Bulk microphysics simulations. *Journal of the Atmospheric Sciences*, *74*(1), 259–273. https://doi.org/10.1175/JAS-D-15-0383.1

Igel, A. L., & van den Heever, S. C. (2017b). The Importance of the Shape of Cloud Droplet Size Distributions in Shallow Cumulus Clouds. Part I: Bin Microphysics Simulations. *Journal of the Atmospheric Sciences*, *74*(1), 249–258. https://doi.org/10.1175/JAS-D-15-0382.1

Igel, A. L., & Van Den Heever, S. C. (2017c). The role of the gamma function shape parameter in determining differences between condensation rates in bin and bulk microphysics schemes. *Atmospheric Chemistry and Physics*, *17*(7), 4599–4609. https://doi.org/10.5194/acp-17-4599-2017

Jensen, M. P., Toto, T., Troyan, D., Ciesielski, P. E., Holdridge, D., Kyrouac, J., Schatz, J., Zhang, Y., & Xie, S. (2015). The Midlatitude Continental Convective Clouds Experiment (MC3E) sounding network: operations, processing and analysis. *Atmospheric Measurement Techniques*, *8*(1), 421–434. https://doi.org/10.5194/amt-8-421-2015

Khain, A. P., Beheng, K. D., Heymsfield, A., Korolev, A., Krichak, S. O., Levin, Z., Pinsky, M., Phillips, V., Prabhakaran, T., Teller, A., van den Heever, S. C., & Yano, J.-I. (2015). Representation of microphysical processes in cloud-resolving models: Spectral (bin) microphysics versus bulk parameterization. *Reviews of Geophysics*, *53*(2), 247–322. https://doi.org/10.1002/2014RG000468

Khain, A., Pokrovsky, A., Pinsky, M. B., Seifert, A., & Phillips, V. (2004). Simulation of Effects of Atmospheric Aerosols on Deep Turbulent Convective Clouds Using a Spectral Microphysics Mixed-Phase Cumulus Cloud Model. Part I: Model Description and Possible Applications. *Journal of the Atmospheric Sciences*, *61*(24), 2963–2982. https://doi.org/10.1175/JAS-3350.1

Koenig, J. L. R., & Murray, F. W. (1976). American Meteorological Society Ice-Bearing Cumulus Cloud Evolution : Numerical Simulation and General Comparison Against Observations. *Journal of Applied Meteorology*, *15*(7), 747–762.

Lin, Y.-L., Farley, R. D., & Orville, H. D. (1983). Bulk Parameterization of the Snow Field in a Cloud Model. *Journal of Climate and Applied Meteorology*, *22*(6), 1065–1092. https://doi.org/10.1175/1520-0450(1983)022<1065:BPOTSF>2.0.CO;2

Marinescu, P. J., van den Heever, S. C., Saleeby, S. M., Kreidenweis, S. M., & DeMott, P. J. (2017). The microphysical roles of lower-tropospheric versus midtropospheric aerosol particles in mature-stage MCS precipitation. *Journal of the Atmospheric Sciences*, *74*(11), 3657–3678. https://doi.org/10.1175/JAS-D-16-0361.1

Marshall, J. S., & Palmer, W. M. K. (1948). THE DISTRIBUTION OF RAINDROPS WITH SIZE. *Journal of Meteorology*, *5*(4), 165–166. https://doi.org/10.1175/1520-0469(1948)005<0165:TDORWS>2.0.CO;2

Meyers, M. P., Walko, R. L., Harrington, J. Y., & Cotton, W. R. (1997). New RAMS cloud microphysics parameterization. Part II: The two-moment scheme. *Atmospheric Research*, *45*(1), 3–39. https://doi.org/10.1016/S0169-8095(97)00018-5

Milbrandt, J. A., & Yau, M. K. (2005a). A Multimoment Bulk Microphysics Parameterization. Part I: Analysis of the Role of the Spectral Shape Parameter. *Journal of the Atmospheric Sciences*, *62*(9), 3051–3064. https://doi.org/10.1175/JAS3534.1

Milbrandt, J. A., & Yau, M. K. (2005b). A Multimoment Bulk Microphysics Parameterization. Part II: A Proposed Three-Moment Closure and Scheme Description. *Journal of the Atmospheric Sciences*, *62*(9), 3065–3081. https://doi.org/10.1175/JAS3535.1

Milbrandt, J. A., Morrison, H., Dawson II, D. T., & Paukert, M. (2021). A Triple-Moment Representation of Ice in the Predicted Particle Properties (P3) Microphysics Scheme. *Journal of the Atmospheric Sciences*, *78*(2), 439–458. https://doi.org/10.1175/JAS-D-20-0084.1

Morales, A., Morrison, H., & Posselt, D. J. (2018). Orographic precipitation response to microphysical parameter perturbations for idealized moist nearly neutral flow. *Journal of the Atmospheric Sciences*, *75*(6), 1933–1953. https://doi.org/10.1175/JAS-D-17-0389.1

Morrison, H., Thompson, G., & Tatarskii, V. (2009). Impact of Cloud Microphysics on the Development of Trailing Stratiform Precipitation in a Simulated Squall Line: Comparison of One- and Two-Moment Schemes. *Monthly Weather Review*, *137*(3), 991–1007. https://doi.org/10.1175/2008MWR2556.1

Morrison, H., Tessendorf, S. A., Ikeda, K., & Thompson, G. (2012). Sensitivity of a simulated midlatitude squall line to parameterization of raindrop breakup. *Monthly Weather Review*, *140*(8), 2437–2460. https://doi.org/10.1175/MWR-D-11-00283.1

Niu, S., Jia, X., Sang, J., Liu, X., Lu, C., & Liu, Y. (2010). Distributions of Raindrop Sizes and Fall Velocities in a Semiarid Plateau Climate: Convective versus Stratiform Rains. *Journal*

of Applied Meteorology and Climatology, *49*(4), 632–645. https://doi.org/10.1175/2009JAMC2208.1

Park, J. M., van den Heever, S. C., Igel, A. L., Grant, L. D., Johnson, J. S., Saleeby, S. M., … Reid, J. S. (2020). Environmental Controls on Tropical Sea Breeze Convection and Resulting Aerosol Redistribution. *Journal of Geophysical Research: Atmospheres*, *125*(6), 1–22. https://doi.org/10.1029/2019JD031699

Petersen, W., L. Carey, V.N. Bringi, A. Tokay, and P. Gatlin. 2011. GPM Ground Validation Two-Dimensional Video Disdrometer (2DVD) MC3E. Data set available online [http://ghrc.nsstc.nasa.gov/] from the NASA EOSDIS Global Hydrology Resource Center Distributed Active Archive Center Huntsville, Alabama, U.S.A. doi: http://dx.doi.org/10.5067/GPMGV/MC3E/2DVD/DATA301

Riley Dellaripa, E. M., Maloney, E. D., Toms, B. A., Saleeby, S. M., & van Den Heever, S. C. (2020). Topographic effects on the Luzon diurnal cycle during the BSISO. *Journal of the Atmospheric Sciences*, *77*(1), 3–30. https://doi.org/10.1175/JAS-D-19-0046.1

Rutledge, S. A., & Hobbs, P. V. (1984). The Mesoscale and Microscale Structure and Organization of Clouds and Precipitation in Midlatitude Cyclones. XII: A Diagnostic Modeling Study of Precipitation Development in Narrow Cold-Frontal Rainbands. *Journal of the Atmospheric Sciences*, *41*(20), 2949–2972. https://doi.org/10.1175/1520-0469(1984)041<2949:TMAMSA>2.0.CO;2

Saleeby, S. M., Herbener, S. R., van den Heever, S. C., & L'Ecuyer, T. (2015). Impacts of Cloud Droplet–Nucleating Aerosols on Shallow Tropical Convection. *Journal of the Atmospheric Sciences*, *72*(4), 1369–1385. https://doi.org/10.1175/jas-d-14-0153.1

Saleeby, S. M., & Van den Heever, S. C. (2013). Developments in the CSU-RAMS aerosol model: Emissions, nucleation, regeneration, deposition, and radiation. *Journal of Applied Meteorology and Climatology*, *52*(12), 2601–2622. https://doi.org/10.1175/JAMC-D-12-0312.1

Saleeby, S. M., Dolan B., Bukowski J., Van Valkenburg K., van den Heever S.C., and Rutledge S. A., 2021: Assessment and limitations of parameterized raindrop breakup in numerical models of cloud microphysics. *J. Geophys. Res.* In Preparation.

Schumacher, R. S. (2017). Heavy Rainfall and Flash Flooding. In *Oxford Research Encyclopedia of Natural Hazard Science* (pp. 1–40). Oxford University Press. https://doi.org/10.1093/acrefore/9780199389407.013.132

Seifert, A., & Beheng, K. D. (2006). A two-moment cloud microphysics parameterization for mixed-phase clouds. Part 1: Model description. *Meteorology and Atmospheric Physics*, *92*(1–2), 45–66. https://doi.org/10.1007/s00703-005-0112-4

Seifert, A. (2008). On the Parameterization of Evaporation of Raindrops as Simulated by a One-Dimensional Rainshaft Model. *Journal of the Atmospheric Sciences*, *65*(11), 3608–3619. https://doi.org/10.1175/2008JAS2586.1

Sheffield, J., & Wood, E. F. (2008). Projected changes in drought occurrence under future global warming from multi-model, multi-scenario, IPCC AR4 simulations. *Climate Dynamics*, *31*(1), 79–105. https://doi.org/10.1007/s00382-007-0340-z

Stevens, B., Ackerman, A. S., Albrecht, B. A., Brown, A. R., Chlond, A., Cuxart, J., … Stevens, D. E. (2001). Simulations of Trade Wind Cumuli under a Strong Inversion. *Journal of the Atmospheric Sciences*, *58*(14), 1870–1891. https://doi.org/10.1175/1520-0469(2001)058<1870:SOTWCU>2.0.CO;2

Storer, R. L., van den Heever, S. C., & Stephens, G. L. (2010). Modeling Aerosol Impacts on Convective Storms in Different Environments. *Journal of the Atmospheric Sciences*, *67*(12), 3904–3915. https://doi.org/10.1175/2010JAS3363.1

Thomas, C. (1994). Water in crisis: a guide to the world's fresh water resources. *International Affairs*, *70*(3), 557–557. https://doi.org/10.2307/2623756

Thompson, G., Field, P. R., Rasmussen, R. M., & Hall, W. D. (2008). Explicit Forecasts of Winter Precipitation Using an Improved Bulk Microphysics Scheme. Part II: Implementation of a New Snow Parameterization. *Monthly Weather Review*, *136*(12), 5095–5115. https://doi.org/10.1175/2008MWR2387.1

Thurai, M., & Bringi, V. N. (2018). Application of the generalized gamma model to represent the full rain drop size distribution spectra. *Journal of Applied Meteorology and Climatology*, *57*(5), 1197–1210. https://doi.org/10.1175/JAMC-D-17-0235.1

Uijlenhoet, R., Steiner, M., & Smith, J. A. (2003). Variability of Raindrop Size Distributions in a Squall Line and Implications for Radar Rainfall Estimation. *Journal of Hydrometeorology*, *4*(1), 43–61. https://doi.org/10.1175/1525-7541(2003)004<0043:VORSDI>2.0.CO;2

Walko, R. L., Cotton, W. R., Meyers, M. P., & Harrington, J. Y. (1995). New RAMS cloud microphysics parameterization part I: the single-moment scheme. *Atmospheric Research*, *38*(1), 29–62.

Wang, D., & Bartholomew, M. J. (2014). Video Disdrometer (VDIS) during ENA. Atmospheric Radiation Measurement (ARM) user facility. Doi: 10.5439/1025315.

Wang, Y., Zheng, G., Jensen, M. P., Knopf, D. A., Laskin, A., Matthews, A. A., Mechem, D., Mei, F., Moffet, R., Sedlacek, A. J., Shilling, J. E., Springston, S., Sullivan, A., Tomlinson, J., Veghte, D., Weber, R., Wood, R., Zawadowicz, M. A., & Wang, J. (2021). Vertical profiles of trace gas and aerosol properties over the eastern North Atlantic: variations with season and synoptic condition. *Atmospheric Chemistry and Physics*, *21*(14), 11079–11098. https://doi.org/10.5194/acp-21-11079-2021

Weisman, M. L., & Klemp, J. B. (1982). The Dependence of Numerically Simulated Convective Storms on Vertical Wind Shear and Buoyancy. *Monthly Weather Review*, *110*(6), 504–520. https://doi.org/10.1175/1520-0493(1982)110<0504:TDONSC>2.0.CO;2

Xue, M., Droegemeier, K. K., Wong, V., Shapiro, A., Brewster, K., Carr, F., Weber, D., Liu, Y., & Wang, D. (2000). The Advanced Regional Prediction System (ARPS) - A multi-scale nonhydrostatic atmospheric simulation and prediction tool. Part II: Model physics and applications. *Meteorology and Atmospheric Physics*, *76*(1–4), 143–165. https://doi.org/10.1007/s007030170027

Xue, H., Feingold, G., & Stevens, B. (2008). Aerosol Effects on Clouds, Precipitation, and the Organization of Shallow Cumulus Convection. *Journal of the Atmospheric Sciences*, *65*(2), 392–406. https://doi.org/10.1175/2007JAS2428.1